

Aerodynamic interaction between propellers of a distributed-propulsion system in forward flight

de Vries, Reynard; van Arnhem, Nando; Sinnige, Tomas; Vos, Roelof; Veldhuis, Leo L.M.

DOI

[10.1016/j.ast.2021.107009](https://doi.org/10.1016/j.ast.2021.107009)

Publication date

2021

Document Version

Final published version

Published in

Aerospace Science and Technology

Citation (APA)

de Vries, R., van Arnhem, N., Sinnige, T., Vos, R., & Veldhuis, L. L. M. (2021). Aerodynamic interaction between propellers of a distributed-propulsion system in forward flight. *Aerospace Science and Technology*, 118, Article 107009. <https://doi.org/10.1016/j.ast.2021.107009>

Important note

To cite this publication, please use the final published version (if applicable). Please check the document version above.

Copyright

Other than for strictly personal use, it is not permitted to download, forward or distribute the text or part of it, without the consent of the author(s) and/or copyright holder(s), unless the work is under an open content license such as Creative Commons.

Takedown policy

Please contact us and provide details if you believe this document breaches copyrights. We will remove access to the work immediately and investigate your claim.



Aerodynamic interaction between propellers of a distributed-propulsion system in forward flight



Reynard de Vries*, Nando van Arnhem, Tomas Sinnige, Roelof Vos, Leo L.M. Veldhuis

Delft University of Technology, Delft, South-Holland, 2629HS, the Netherlands

ARTICLE INFO

Article history:

Received 7 April 2021

Received in revised form 18 June 2021

Accepted 31 July 2021

Available online 9 August 2021

Communicated by George Barakos

Keywords:

Distributed propulsion

Propeller performance

Propeller interaction

Experimental aerodynamics

ABSTRACT

This article describes an experimental investigation of the aerodynamic interaction that occurs between distributed propellers in forward flight. To this end, three propellers were installed in close proximity in a wind tunnel, and the changes in their performance, flow-field characteristics, and noise production were quantified using internal force sensors, total-pressure probes, particle-image velocimetry (PIV), and microphones recessed in the wind-tunnel wall. At the thrust setting corresponding to maximum efficiency, the efficiency of the middle propeller is found to drop by 1.5% due to the interaction with the adjacent propellers, for a tip clearance equal to 4% of the propeller radius. For a given blade-pitch angle, this performance penalty increases with angle of attack, decreasing thrust setting, or a more upstream propeller position, while being insensitive to the rotation direction and relative blade phase angle. Furthermore, the velocities induced by the adjacent propeller slipstreams lead to local loading variations on the propeller disk of 5% – 10% of the average disk loading. Exploratory noise measurements show that the interaction leads to different tonal noise waveforms of the system when compared to the superposition of isolated propellers. Moreover, the results confirm that an active control of the relative blade phase angles between propellers can effectively modify the directivity pattern of the system.

© 2021 The Author(s). Published by Elsevier Masson SAS. This is an open access article under the CC BY-NC-ND license (<http://creativecommons.org/licenses/by-nc-nd/4.0/>).

1. Introduction

The development of novel propulsion systems with increased efficiency is a key research area required to limit the climate impact of aviation [1–3]. In recent years, the amount of research focused on (hybrid-)electric propulsion has surged [4,5] since, among other things, it enables distributed-propulsion arrangements with improved aerodynamic or propulsive efficiency [6]. This has led to the appearance of aircraft concepts featuring numerous, electrically-driven propellers, typically placed side-by-side above [7] or ahead of [8–10] the wing. These propellers are installed in close proximity to each other, either due to geometrical constraints, or to enhance the lift-to-drag ratio [11] or high-lift capabilities [12] of the wing as much as possible, without much regard for potential interference effects among the propellers. Although closely-placed propellers have been used successfully on several aircraft throughout the past century (see for example, the Dornier Do-X [13]), the appearance of distributed-propulsion configurations requires a more in-depth analysis of the interaction between such propellers. This is because the aerodynamic inter-

action plays a relatively larger role in the performance of these highly-integrated propulsion systems, and the aero-propulsive efficiency must be increased substantially in order to offset the weight of the (hybrid-) electric drivetrain and make such configurations feasible [14].

A significant amount of literature is available regarding the aerodynamic interaction between two or more rotors in the case of tandem helicopters [15–17], tiltrotors [18,19], small unmanned aerial vehicles (UAVs or “drones”) [20–30], and urban air mobility (UAM) vehicles [31,32]. Based on these studies, where the “propellers” operate at or near to zero forward velocity, it becomes evident that the aerodynamic interaction between adjacent rotors is relevant in three main ways:

1. The performance of the rotors themselves is affected. When placed close to each other without overlap, the thrust produced at a given rotational speed typically drops by 2% – 8% [21,22,24,30], depending on the configuration, and the efficiency is reduced [16]. For propellers in forward flight, this penalty would increase with sideslip [31]. Moreover, the interaction leads to an appreciable unsteady loading on the propeller blades [21,23,25].

* Corresponding author.

E-mail address: R.deVries@tudelft.nl (R. de Vries).

by the interaction with its neighbors, without including additional interaction mechanisms with the rest of the airframe. The measurement techniques employed are described along with the experimental setup in Sec. 2. Section 3 then discusses how the flow field upstream and downstream of the propeller is affected by the adjacent propellers, and how this relates to propeller performance. Subsequently, Sec. 4 presents how these interaction effects vary with different parameters such as the rotation direction, angle of attack, axial position, differential-thrust settings, or relative blade-phase angle. Finally, a preliminary discussion of the impact of the interaction effects and relative blade-phase angle on noise production is provided in Sec. 5.

2. Experimental setup

2.1. Facility and model description

The experiments were performed at the low-speed, low-turbulence tunnel (LTT) at Delft University of Technology. This closed-circuit wind tunnel presents a maximum freestream velocity of 120 m/s, with turbulence levels below 0.04% for the freestream velocity considered in this experiment [45]. The test section has an octagonal cross-section of 1.25 m x 1.8 m, as depicted in Fig. 1a. An array of three propellers was used in the setup, so that the flow conditions perceived by the middle propeller were representative of a distributed-propulsion configuration. Since the influence of one propeller on another decreases rapidly with separation distance [22,24,25], the influence of additional, more distant propellers on the middle propeller is a second-order effect, and thus the quasi-periodicity condition can be approximated by placing just one propeller on each side. These six-bladed, steel propellers have a radius of $R = 101.6$ mm and are known as the “XPROP-S” propellers, whose blade chord and pitch distributions are given in Fig. 2. Additional characteristics of the propellers can be found in earlier studies [46–48]. Additionally, a fourth, mirrored version of the propeller was used to be able to change the rotation direction of the middle propeller and replicate a counter-rotating configuration (Fig. 1b). These propellers were installed on a straight, untapered support sting consisting of a NACA 0020 profile with an original airfoil chord of 100 mm, but with the last two millimeters truncated for manufacturability reasons. The leading edge was located approximately $3R$ downstream of the propeller disks, to limit the upstream influence on the propellers.

The propellers were driven by brushless DC electrical motors, each powered by a dedicated PWM-controlled trapezoidal electronic speed controller (ESC) and an externally programmable 5 kW DC power supply. The electrical motors were housed inside an aluminum nacelle, which could be fixed at different spanwise locations on the support sting in order to vary the separation distance between the propellers. The left and right nacelles could be removed and replaced with caps to minimize the influence on the middle propeller during “isolated” propeller measurements, as shown in Fig. 1c. Moreover, several inserts could be installed in the nacelles to vary their length and therewith change the stagger of the propellers; that is, to change their relative axial position (Figs. 1d–1g).

2.2. Test conditions & configurations

Measurements were performed at a nominal freestream velocity of $V_\infty = 30$ m/s, with a propeller blade pitch of $30^\circ \pm 0.05^\circ$ at 70% of the blade radius. The blade pitch angle is such that the maximum efficiency is obtained at a high thrust setting, and is therefore more representative of take-off conditions than of cruise conditions. This setting was preferred over larger pitch angles since higher thrust coefficients and blade tip Mach numbers could be

achieved, which made both the aerodynamic and acoustic interaction effects more clearly identifiable in the experiment. The propellers were evaluated for advance ratios ranging from $J = 0.8$ (184.5 Hz) to $J = 1.35$ (109.3 Hz), as reflected in Table 1. This corresponds to thrust coefficients T_C between 0 and 1.1, blade tip Mach numbers ranging from 0.22 to 0.36, and a blade Reynolds number at 70% radius ranging from approximately $3.8 \cdot 10^4$ to $6.0 \cdot 10^4$. In addition to testing the “distributed” and “isolated” propeller configurations, several measurements were performed with a single propeller installed on one of the three nacelles, to distinguish the interaction with adjacent propellers from the interaction with adjacent nacelles.

The rotational speed of the propellers was controlled with custom-made software, achieving a standard deviation of the rotational speed of 0.1 Hz during random-phase measurements, and of 0.05 Hz during phase-controlled measurements. The random-phase measurements were performed by increasing the rotational speed of the two outer propellers by 0.03 Hz relative to the center propeller, such that the relative blade angles between the propellers $\Delta\phi$ would cover approximately one blade passage (0° to 60°) throughout the acquisition time of each measurement point. Thus, the averaged reading represents a phase-random measurement. This offset in rotational speed corresponded to a change in advance ratio below 0.03%, and therefore had a negligible effect on (isolated) propeller performance. In the phase-controlled measurements, the blade position of the two outer propellers was controlled relative to the blade position of the middle propeller, and the performance and noise production of the system was evaluated in steps of 10° (see Table 1). The standard deviation of the relative blade-phase angle during these measurements was below 0.3° . Therefore, the controller was sufficiently accurate to study the effect of the relative blade-phase angles on noise production without any appreciable loss in coherence of the noise sources [37].

Additionally, the angle of attack, rotation direction, tip clearance, and stagger of the propellers was varied. The angle of attack α could be set with an accuracy of $\pm 0.1^\circ$, which was the maximum difference in installation angle observed among the three propellers and the horizontal axis (at $\alpha = 0^\circ$) in repeated installation procedures. Regarding the tip clearance between adjacent propellers, most measurements were performed at a small separation distance ($d/R = 0.04$), since numerous previous studies have already shown that the interaction effects are strongest at small separation distances, and rapidly reduce as the separation distance increases [22,24,25]. To decouple the noise contribution of the interaction effects from the superimposed contribution of the three individual propellers, a subset of measurements was performed at a large tip clearance ($d/R = 1.00$) in order to minimize the aerodynamic interference. Repeated installation procedures showed that the tip clearance varied by less than ± 0.5 mm ($d/R \pm 0.005$) among the different measurements of a determined d/R setting. Finally, the relative axial position of the propellers could be accurately changed by including one or more inserts of 20 mm length in each nacelle. These inserts were used to simulate the three configurations shown in Figs. 1e–1g, in addition to the baseline, zero-stagger configuration. A summary of these parameters is given in Table 1. The results discussed in Secs. 3–5 are presented for the baseline parameter values, unless explicitly mentioned otherwise.

2.3. Measurement techniques

This section describes the four types of measurement performed. For the normalization of the recorded performance and flow-field parameters, the effective freestream velocity was corrected for nacelle, support-sting, and slipstream blockage. The blockage effect of the nacelles and support sting at the center of the middle propeller was estimated numerically by representing

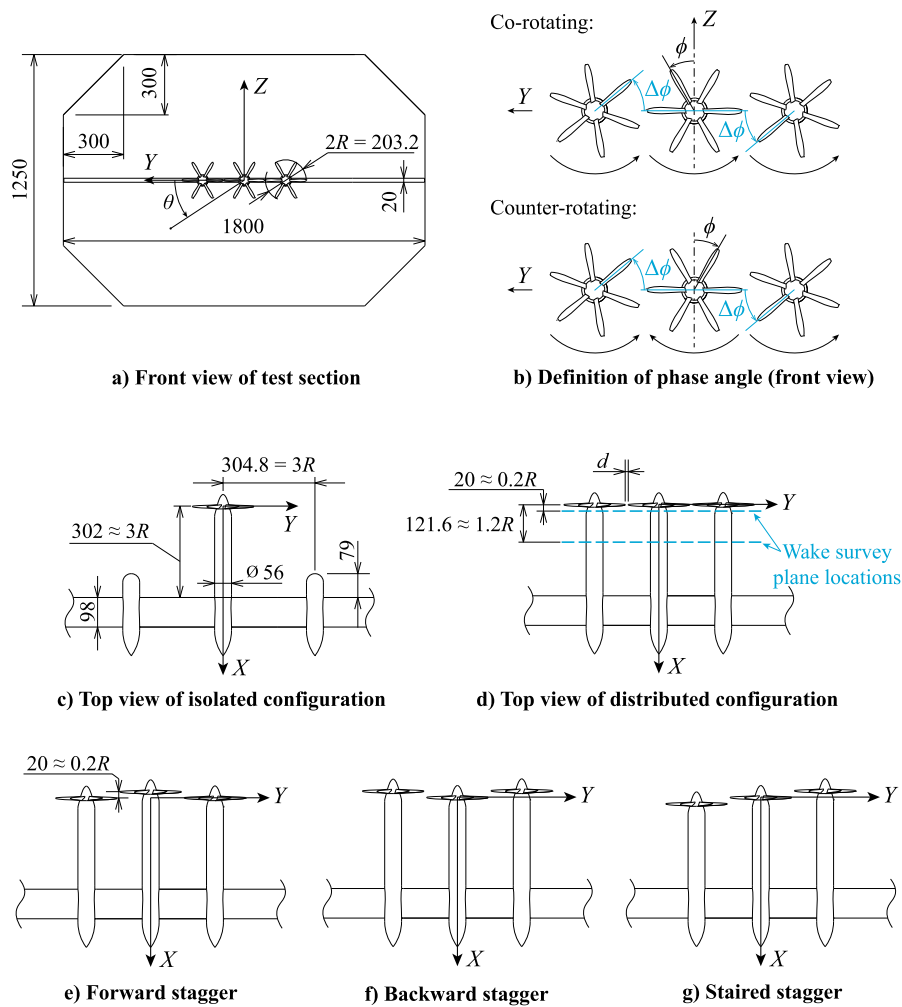


Fig. 1. Overview of test setup, indicating main dimensions, reference systems, and configurations. Dimensions in mm.

Table 1
Overview of test conditions.

Parameter	Evaluated values	Baseline value
Freestream velocity V_∞ [m/s]	30	30
Blade pitch at $r/R = 0.7$ [deg]	30	30
Advance ratio J [-]	$0.80 < J < 1.35$ ($1.1 > T_c > 0$)	1.00 ($T_c \approx 0.45$)
(P)ropeller/(N)acelle configuration	3P + 3N ("distributed"), 1P + 3N, 1P + 1N ("isolated")	3P + 3N
Relative blade-phase angle $\Delta\phi$ [deg]	random, 0, 10, 20, 30, 40, 50, 60	random
Rotation direction	co-rotating, counter-rotating	co-rotating
Angle of attack α [deg]	0, 5	0
Tip clearance d/R [-]	0.04, 1.00	0.04
Stagger $\Delta X/R$ (left, mid, right) [-]	in-line (0, 0, 0), forward (0, 0.2, 0), backward (0.2, 0, 0.2), staired (0, 0.2, 0.4)	in-line (0, 0, 0)

them as a distribution of point sources and placing image sources to mimic the wind-tunnel walls, as recommended in Ref. [49]. Glauert's slipstream blockage correction was applied to account for propeller thrust. Combined, the effect of blockage was found to range between -0.5% and $+1.0\%$ of the nominal freestream velocity, depending on the configuration and thrust setting.

2.3.1. Load measurements

The middle propeller was instrumented with an ATI MINI-40E six-component force sensor to measure forces and moments on the propeller (i.e., on the blades and spinner). The force sensor was calibrated for a full-scale load range of 60 N, 20 N, and 1 Nm for thrust, in-plane forces, and torque, respectively. For each configuration, propeller forces were measured for several advance ratios (see

Table 1). Data were sampled at 10 kHz and averaged over 5 seconds. In every measurement run, each advance-ratio setpoint was measured at least four times, and the measurement sequence was randomized to convert potential systematic errors within a measurement run (i.e., drifts) into random error. Additionally, repeated measurements were performed after several days and configuration changes for selected cases to verify the reproducibility of results. The differences between repeated measurement runs were found to be comparable to the scatter observed within a single run. Third-order polynomial fits were made through the thrust and torque curves to model the propeller response over the considered advance-ratio range.

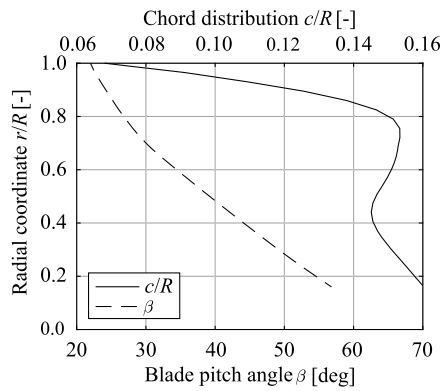


Fig. 2. Blade chord and pitch distributions of the six-bladed XPROP-S propeller. Figure adapted from Ref. [46].

The uncertainty of the performance curves was estimated taking into account potential misalignments in propeller angle-of-attack, errors in the temperature-calibration factors (see following paragraphs), and random error in the data due to e.g. variations in operating conditions. The resulting errorbars are included in performance curves throughout this article. These errorbars present the 95% confidence interval for a determined propeller geometry. They do not include potential errors due to deviations in blade geometry from the theoretical blade shape, or misalignments in blade-pitch angle. A comparison of the four, theoretically identical propellers showed deviations of approximately $T_c \pm 0.005$ and $Q_c \pm 0.0005$ between each other. This error has a second-order, negligible effect on the changes in performance reported in this article, but should be taken into account when comparing the absolute performance of the propeller to numerical simulations with idealized geometries.

Furthermore, the variations in motor temperature were found to appreciably affect the load-cell readings, and therefore a linear temperature calibration was applied, similarly to Ref. [47]. In order to verify that the temperature calibration was performed correctly, the force components obtained from the internal sensor were cross-validated with those obtained using an external balance, on which the support sting was installed. This balance had an uncertainty of ± 0.02 N in the considered measurement range, and could be used to measure propeller thrust by subtracting the axial force measured with the propeller off from the one measured with the propeller on. For these “propeller off” measurements, the propeller was removed and replaced by a dummy spinner without blades. The net thrust obtained from the external balance therefore included the thrust on the blades and the changes in interference drag on the support sting, nacelle, and spinner due to the propeller slipstream.

The propeller thrust curves obtained from the two methods are compared in Fig. 3. For the internal force sensor, the thrust was the force component most sensitive to temperature variations. A minor slope difference can be observed between the external balance and internal force-sensor data, suggesting that the interference drag recorded by the external balance increased with propeller thrust. Nevertheless, the two techniques show an acceptable agreement, indicating that either the interference drag and temperature-calibration effects were both small, or that they both led to a comparable deviation from the true propeller thrust. The interference-drag contribution was estimated to be below 2% of the propeller thrust at the baseline $T_c = 0.45$, based on the total-pressure and swirl-angle distributions of the isolated propeller slipstream (shown in Sec. 3.2). Moreover, repeated internal force-sensor measurements at different motor temperatures led to similar results. Thus, it was concluded that the temperature calibration process provided reliable values of the propeller performance.

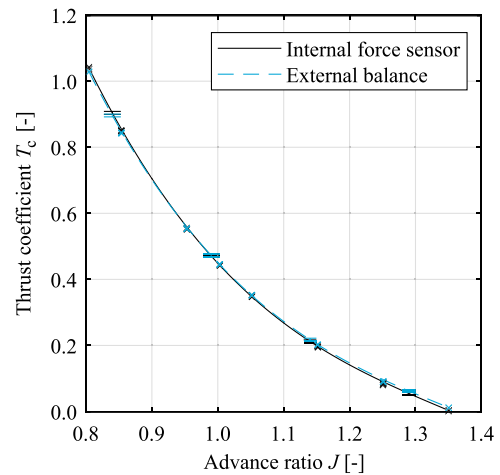


Fig. 3. Comparison of the isolated propeller thrust, as obtained from the external balance and internal force sensor. Markers indicate individual measurements.

2.3.2. Wake-pressure measurements

The total-pressure distribution behind the propellers was measured at two locations: close to the propeller ($X/R = 0.2$), which reflects the non-uniform loading distribution on the propeller disk, and further downstream ($X/R = 1.2$), to determine whether the slipstreams had deformed significantly at a typical wing leading-edge location. The wake pressures were measured for the configurations shown in Figs. 1c–1f, and the position of the two survey planes is shown in Fig. 1d. For this, two types of probes were used. Firstly, a single Pitot probe was traversed horizontally in the Y -direction ($Z/R = 0$) directly behind the propeller, with a spatial resolution ranging from 3 mm in the inboard region to 0.5 mm in the blade-tip region. This provided an appropriately resolved total-pressure distribution and location of the slipstream edge. Secondly, a vertical wake rake containing 74 total-pressure probes, separated 3 mm, was traversed in Y -direction behind the propellers, also in steps of 3 mm. This provided a two-dimensional pressure distribution of the flow field, though with reduced resolution compared to the single probe.

The pressure ports were connected to an electronic pressure scanner. The pressure sensors present an uncertainty of ± 4 Pa on the full-scale measurement range, corresponding to $\pm 0.7\%$ of the freestream dynamic pressure. Repeated measurements showed only minor quantitative differences (± 2 Pa), and no qualitative differences. Each data point was averaged over 10 seconds measurement time, at an acquisition frequency of 10 Hz.

2.3.3. Particle-image velocimetry

A stereoscopic particle-image velocimetry (PIV) setup was used to obtain the velocity distributions upstream and downstream of the propellers. For this, a query plane was set up parallel to the XZ plane in between two of the propellers, as shown in Fig. 4. A mixture of diethylene-glycol and water was used for flow seeding, obtaining tracer particles with an average diameter and relaxation time below 1 μm and 1 μs , respectively. A 200 mJ Nd:YAG laser was used for illumination, positioned beneath the test section. The light was directed through a plexiglass plate in the wind-tunnel floor, generating a laser sheet of approximately 2 mm thickness upstream and downstream of the propellers. Four 16-bit LaVision Imager sCMOS cameras were used for image acquisition, two for the field-of-view (FOV) upstream of the propellers, and two for the FOV downstream of the propellers. These cameras feature a 2560×2160 pixel sensor with a pixel size of 6.5 μm , and were equipped with 105 mm lenses at $f/11$ aperture.

The images were recorded at 15 Hz and processed using LaVision Davis 8.4 software. For each measurement, 500 uncorrelated

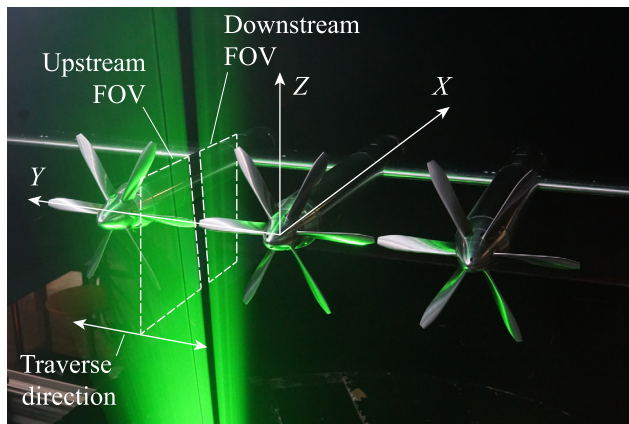


Fig. 4. Position of the fields of view (FOV) in the PIV setup.

Table 2
Main characteristics of the PIV setup.

FOV	Upstream	Downstream
Field of view $X \times Z$ [mm ²]	100 × 120	100 × 160
Number of (uncorrelated) images [-]		500
Number of parallel planes [-]		26
Plane locations [mm]	$Y \in [51.6, 145.2]$	
Focal length [mm]		105
Pixel shift [pixel] (at V_∞)		10
Imaging resolution [pixel/mm]		16.8
Window size [pixel ²]	64 × 64	
Overlap factor [%]	50	
Vector spacing [mm]	1.9	
Instantaneous velocity uncertainty [%]	1.3 ^a	3.7 ^b
Mean velocity uncertainty [%]	0.1 ^a	0.2 ^b

^a Average value upstream of propeller disk, as a percentage of V_∞ .

^b Average value in tip-vortex region, as a percentage of V_∞ .

images were acquired. By traversing the cameras and laser in Y direction, multiple parallel planes were sampled, evaluating a total of 26 planes in steps of 1.8 mm (in the tip region) to 5 mm (at the more inboard blade locations). A combination of these planes provided volumetric information of the time-averaged velocity field upstream and downstream of the propellers. A summary of the characteristics of the setup is provided in Table 2. The table also includes the uncertainty of the velocity field, computed following the method outlined in Ref. [50]. Note that this uncertainty does not include potential errors due to misalignment of the illumination plane relative to the model, or possible deviations from the nominal test conditions established in Table 1. An inspection of the flow field immediately upstream of the isolated propeller, which in theory should be symmetric with respect to the $Z = 0$ plane, showed differences of up to 2% of the freestream velocity between the upper and lower halves of the FOV. This indicative error band should be taken into account when comparing the results to independent numerical or experimental analyses.

2.3.4. Microphone measurements

Microphone measurements were performed to obtain a preliminary understanding of the noise production of a distributed-propeller system. These measurements should not be used to predict the far-field noise levels of the system, for several reasons. Firstly, the test section was not acoustically treated, and thus significant acoustic reflections could occur on the wind-tunnel walls and support sting. Secondly, the microphones were placed relatively close to the propellers ($\Delta Z/D \approx 3$), and therefore the propellers cannot be treated as distant point sources. Thirdly, only a small portion of the directivity sphere was sampled, and thus no quantitative conclusions can be drawn regarding overall noise

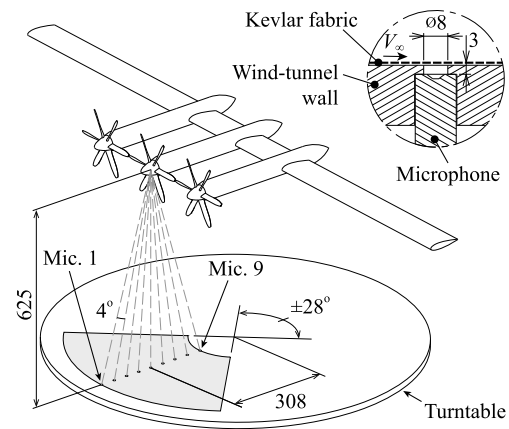


Fig. 5. Location of microphones used for noise measurements, including a close-up of the microphone cavity (top right). Dimensions in mm.

levels in an arbitrary direction. Nevertheless, keeping these limitations in mind, the microphone data provide useful insight into several aspects. Firstly, they demonstrate whether it is possible to control the noise directivity effectively by modifying the relative phase angle between propellers. Moreover, they provide qualitative comparisons of the average noise levels beneath the propellers for different configurations. Furthermore, the spectra and waveforms recorded at different axial and circumferential directivity angles provide an understanding of how the aerodynamic interaction effects identified in the experiment can contribute to the noise production.

To this end, nine microphones were installed along a radius of the turntable in the wind-tunnel floor, as depicted in Fig. 5. The radial location of the microphones was such that the central one was located directly beneath the center of the middle propeller disk. The remaining eight microphones were equally divided upstream and downstream of the center microphone in steps of 4° azimuth relative to the center of the propeller disk. The turntable was rotated around the vertical axis in steps of 2° to record the noise signal on each side of the wind-tunnel centerline. The resulting area covered during the sweeps is notionally indicated in gray in Fig. 5.

Five LinearX M53 (odd locations: microphones 1, 3, 5, 7, 9) and four LinearX M51 (even locations: microphones 2, 4, 6, 8) were used to acquire data. These were installed maintaining a small cavity between the microphone and the wind-tunnel wall, which was covered with Kevlar fabric, as shown in Fig. 5. The M53 and M51 microphones measured in a frequency range of 20 Hz – 20 kHz, with a maximum input level of 130 dB and 150 dB (ref $20 \cdot 10^{-6}$ Pa), and an equivalent noise level of 18 dBA and 34 dBA, respectively. The microphones were calibrated with a piston phone emitting a known signal of 114 dB amplitude at a frequency of 250 Hz. Data were recorded synchronously with the propellers' once-per-revolution trigger signal at a sampling frequency of 51.2 kHz, using a series of 24-bit data-acquisition modules with integrated anti-aliasing filters. The acquisition time of each measurement point was 20 seconds, corresponding to approximately 13,000 to 22,000 blade-passage periods, depending on the rotational speed of the propellers.

For the microphone measurements, no systematic uncertainty analysis was carried out. However, a comparison of repeated measurements showed that the rms of the pressure signal recorded at the blade passage frequency at a determined location could vary by up to 0.15 Pa, which corresponds to approximately 4 dB variation at typical tonal-peak amplitudes. This repeatability margin is higher than the variation observed in previous single-propeller experiments performed in the same wind tunnel [48,51].

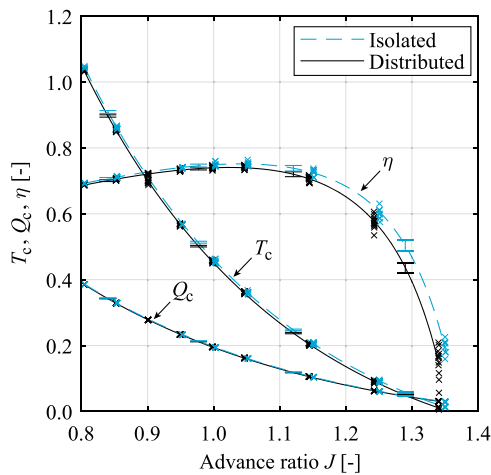


Fig. 6. Performance of the middle propeller in the baseline isolated and distributed configurations. Markers indicate individual measurements.

Given that the broadband levels of the repeated measurements were practically identical, this difference in tonal components was predominantly attributed to the sensitivity of the interference of noise sources to variations in atmospheric conditions, and rotational speed or blade-phase angle [37]. The overall sound pressure level recorded at a determined location was found to be repeatable to within 2.5 dB, and the mean sound pressure level recorded over the entire measurement area (SPL_{mean}^*) deviated by less than 0.5 dB. Moreover, the tonal peak at the blade-passage frequency (BPF) was found to be typically 10–20 dB higher than the broadband noise levels, which were in turn at least 40 dB higher than the background noise levels with the wind tunnel off. These repeatability margins and signal-to-noise ratios indicated that the microphone data was sufficiently accurate to distinguish the differences observed among the various configurations with confidence.

3. Interaction effects in baseline configuration

This section describes the time-averaged aerodynamic interaction observed between the three propellers in the baseline configuration, without stagger or angle-of-attack effects. First, the effect of this interaction on the performance of the propellers is presented in Sec. 3.1. Then, the changes in velocity and pressure fields relative to the isolated-propeller case are described in Sec. 3.2, to explain the changes in propeller loading and slipstream development.

3.1. Propeller performance

To understand the impact of the aerodynamic interaction on propeller performance, Fig. 6 presents the thrust coefficient, torque coefficient, and efficiency of the middle propeller versus advance ratio, for the isolated and distributed-propeller cases. The figure shows a slight reduction in thrust in the distributed-propeller configuration for all advance ratios, which outweighs the reduction in torque and, overall, leads to a drop in propeller efficiency. The efficiency loss is especially evident at high advance ratios. This occurs because the performance loss is predominantly caused by a local variation in effective advance ratio (see Sec. 3.2.1), and the propeller efficiency is more sensitive to variations in advance ratio as the propeller approaches the zero-thrust condition.

Fig. 6 indicates that, for a fixed-pitch propeller, a significant performance loss can occur due to propeller–propeller interaction at low thrust settings. However, in practice, a propeller typically operates at the advance ratio corresponding to maximum efficiency

in cruise conditions, and to the left of that (i.e., at lower advance ratios) in take-off or climb conditions. Therefore, the appreciable efficiency loss visible in Fig. 6 for $J > 1.2$ can be avoided by selecting an appropriate blade-pitch setting. For a variable-pitch propeller, the loss in propeller efficiency at the thrust setting corresponding to maximum efficiency ($T_c \approx 0.38$, in this case) is more representative of the performance loss due to propeller–propeller interaction. In Fig. 6, the propulsive-efficiency penalty at this thrust setting is approximately 1.5% of the isolated-propeller efficiency. The cause of this performance loss is described in the following section.

3.2. Flow-field characterization

The presence of additional propellers alters the inflow conditions to each propeller, thus changing the loading distribution on the propeller blades. This variation in loading affects the velocity and pressure field downstream of the propeller, which is also simultaneously affected by adjacent propeller slipstreams. In order to understand this aerodynamic coupling, Sec. 3.2.1 first describes the flow field upstream of the propellers, and Sec. 3.2.2 subsequently describes the evolution of the flow field downstream of the propellers.

3.2.1. Inflow conditions

Fig. 7 shows how the velocity field ahead of the middle propeller is affected by the presence of adjacent propellers. The velocity distributions are obtained from the ensemble-averaged PIV data, and only a part of the FOV is shown. In this figure, the velocity vectors indicate the in-plane velocities induced by the propellers and nacelles; i.e. the freestream velocity has been subtracted from the axial component. The slipstream contraction is evident in the horizontal plane of the isolated-propeller case (Fig. 7a). Near the radial position of maximum loading ($Y/R \approx 0.7$), the radial velocity is zero, while further outboard, the slipstream contracts. Inboard of $Y/R = 0.7$, on the other hand, the radial flow is outward-oriented. This outward-oriented flow is caused predominantly by the spinner. The trailing vorticity in the inboard region of the blade also plays a minor role, since it is opposite in sign compared to the tip region, and induces radial velocities which cause the streamtube to expand rather than to contract.

When additional propellers are placed on the side (Fig. 7b), two main differences can be observed. Firstly, the velocity magnitude has increased, as can be seen by comparing the contour levels of Figs. 7a and 7b. Secondly, near the propeller tip, the spanwise velocity component v is reduced to practically zero. This is especially evident in the close-up view, where the distributed-propeller velocity vectors (black) are practically aligned in streamwise direction, while the isolated-propeller velocity vectors (white) present a significant spanwise component. Above the horizontal plane ($Z > 0$), the reduction in spanwise velocity is accompanied by an increase in the magnitude of the vertical velocity component w , leading to the reorientation of the velocity vectors indicated in Fig. 7b.

To analyze these differences in more detail, Fig. 8 displays the axial and tangential velocity profiles extracted from the cross-flow plane upstream of the propeller disk at $X/R = -0.2$, for three azimuthal locations. The axial velocity profiles (Fig. 8a) show that the inflow velocity is higher in the distributed configuration than in the isolated configuration, especially along the centerline ($\theta = 0^\circ$). The tangential velocity profiles, on the other hand, show no significant swirl at $\theta = 0^\circ$ in Fig. 8b. This is expected since, in a time-averaged sense, a propeller does not induce swirl upstream of the propeller disk. However, as the blade approaches this horizontal position, it perceives a tangential inflow in the same direction as the blade rotation direction ($\theta = -30^\circ$). On the other hand, once

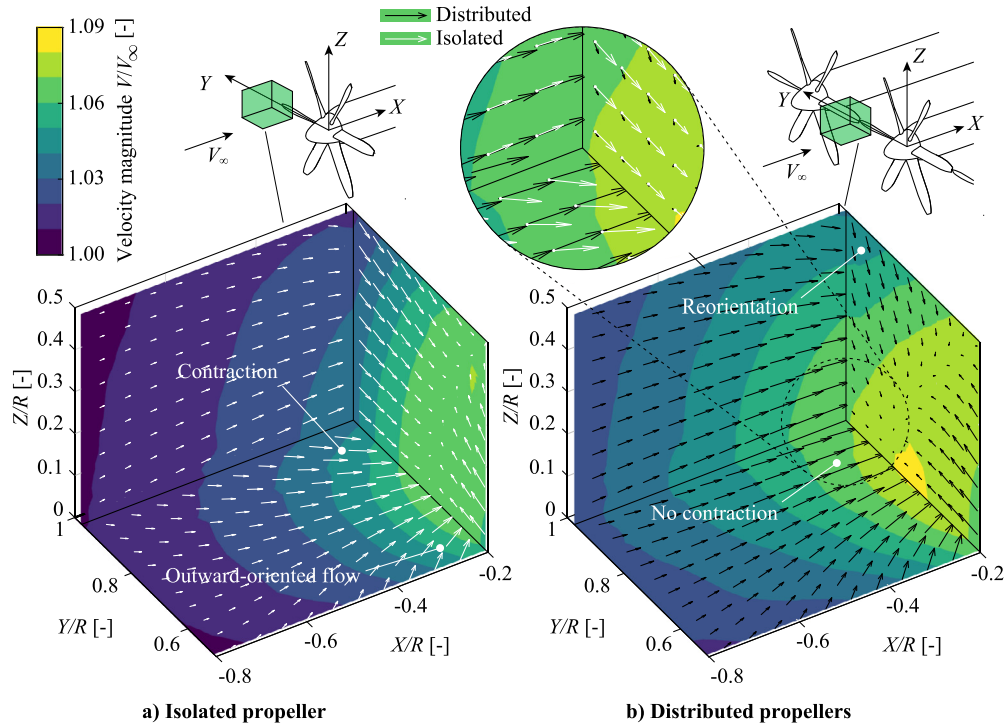


Fig. 7. Inflow velocity distributions upstream of the middle propeller in isolated and distributed configurations. (For interpretation of the colors in the figure(s), the reader is referred to the web version of this article.)

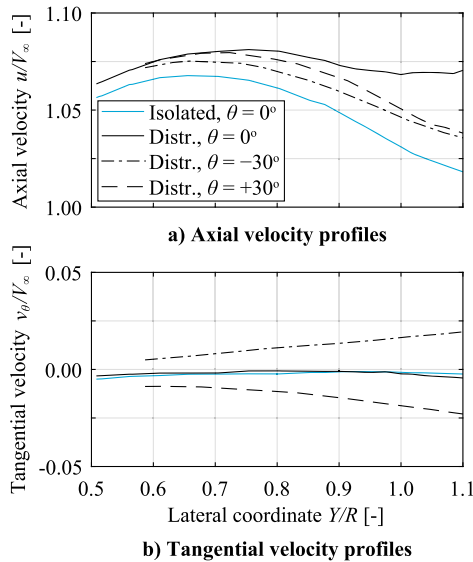


Fig. 8. Axial and tangential velocity profiles upstream of the middle propeller ($X/R = -0.2$), at three azimuthal locations: approaching side ($\theta = -30^\circ$), horizontal position ($\theta = 0^\circ$), and retreating side ($\theta = +30^\circ$).

it passes this horizontal position, it perceives a negative tangential inflow ($\theta = +30^\circ$).

The changes in inflow conditions can be explained by considering the velocities induced by the propeller vortex system. The vortex associated to an idealized single blade without spinner contains three segments: the root vortex (axial), the bound vortex (radial), and the tip vortex (helical). The tip vortex can, in turn, be decomposed into an axial and tangential component. Thus, in a time-averaged sense, the trailing vorticity in the propeller slipstream can be represented by a distribution of axial vorticity lines and tangential vorticity rings [52,53]. This decomposition is indi-

cated in the gray mesh in Fig. 9. It can be shown that, of these components, only the tangential one (Γ_θ) induces axial and radial velocities, while the bound (Γ_{blade}) and axial (Γ_x, Γ_{root}) components only contribute to the swirl velocity behind the propeller disk [54]. Therefore, the changes in inflow conditions observed in Figs. 7 and 8 can be understood by representing the propeller as a semi-infinite series of ring vortices, starting at the propeller location.

The velocity field induced by such a semi-infinite distribution of ring vortices is notionally shown in the lower left corner of Fig. 9. For this illustration, it is assumed that all tangential vorticity is concentrated in the tip (i.e., that the blade loading is constant), and the Biot-Savart law is applied to discretized vortex segments. The illustration shows how the radial velocities are highest at the start of the vortex tube, while decaying to zero in upstream and downstream directions. Inside the vortex tube, the axial velocity gradually increases in streamwise direction, in line with actuator disk theory. Outside the vortex tube, the axial velocity is increased upstream of the propeller disk, decreased downstream of the disk, and is not affected at the disk location. Therefore, a propeller induces both axial and radial velocities ahead of the adjacent propellers.

These induced velocities are shown by the vectors sketched on the two gray planes of Fig. 9, where the black arrows represent the velocity components induced by the middle propeller, and the blue arrows on the left- and right-hand sides represent the velocity components induced by the starboard and port propellers, respectively. The effect of the port and starboard propellers on the opposite sides is neglected for simplicity, since the increased distance makes it a second-order effect. For a point on the horizontal plane halfway between two propellers (right-hand side of Fig. 9), the induced axial velocities u_{ind} add up, while the radial components $v_{r,ind}$ oppose each other. This is the cause for the axial velocity increase observed in Fig. 8a, and the reduction in spanwise velocity observed in Fig. 7b. If a generic azimuthal location θ is analyzed instead (left-hand side of Fig. 9), the velocity induced by the

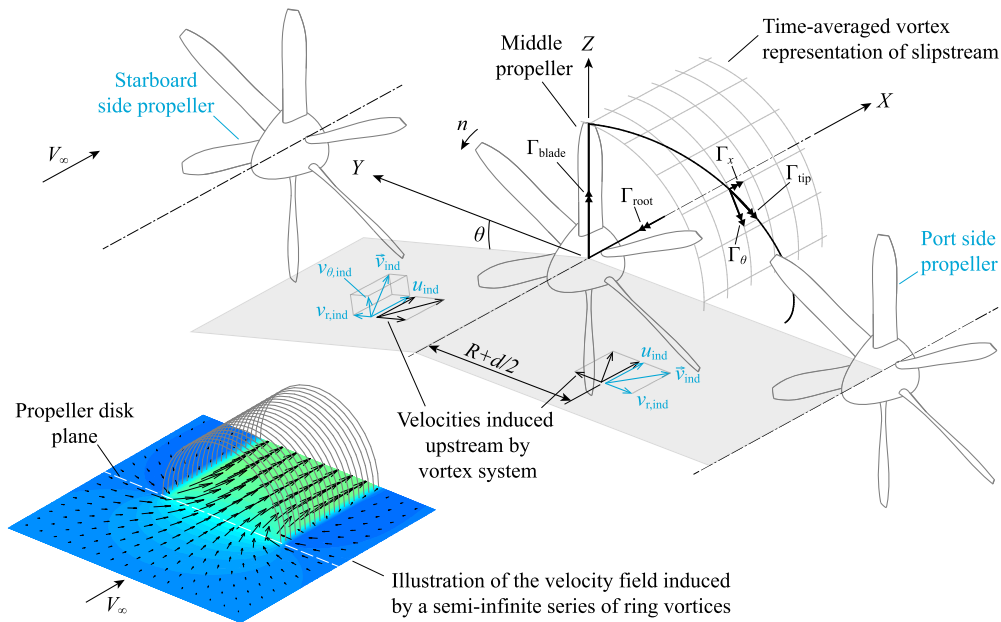


Fig. 9. Conceptual sketch of the propeller vortex system, the velocities it induces, and its effect on the inflow to adjacent propellers.

side propeller not only affects the axial and radial inflow components, but additionally creates an out-of-plane component, $v_{\theta,ind}$. This tangential component is reflected in the profiles of Fig. 8b.

The increase in axial velocity observed upstream of the propeller disk is, however, not the main cause for the loss of thrust in the distributed-propeller configuration: at the propeller disk location, the axial velocity induced by adjacent vortex systems is approximately zero (see illustration in Fig. 9). The tangential inflow component is also not responsible for the thrust loss, since it is symmetric with respect to the $Z = 0$ plane and would, on average, lead to a negligible thrust increase, similar to a propeller at a small angle of attack. Therefore, the thrust reduction is caused by the nacelles. This effect is conceptually indicated in Figs. 10a and 10b. When additional nacelles are installed next to the middle propeller, the inflow velocity increases as a result of the blockage of the nacelles. This was confirmed by comparing thrust measurements with one propeller and three nacelles (not shown here) to those of the isolated propeller. The comparison showed that the majority of the thrust loss occurred when the additional nacelles were installed, while the incorporation of the adjacent propellers themselves had a much smaller effect. For this reason, the two T_C curves of Fig. 6 present a relatively constant offset, rather than a difference in slope.

Although the adjacent propellers' vortex systems do not significantly affect the thrust of the middle propeller, they do lead to unsteady loading. While the inflow conditions of an isolated propeller are axisymmetric, the velocities induced by adjacent propellers break this axisymmetry and create a (quasi-)symmetry plane between each pair of propellers instead, as shown in Figs. 10c and 10d. In a time-averaged sense, this "boundary condition" would represent a perfect symmetry condition if an array of infinite propellers were considered, in which case the spanwise velocity would be exactly zero halfway between each pair of propellers. The associated reorientation of the in-plane Cartesian velocity components (v, w) in the propeller disk leads to the tangential component observed in Fig. 8b, causing a twice-per-revolution excitation on the blades of the middle propeller. It is worth noting that, while the axial velocity induced by the propellers outside the slipstream is zero in the plane of the propeller disk (see bottom left of Fig. 9), the induced radial velocities are highest at that axial location. Therefore, the use of stagger (Sec. 4.3) not only affects

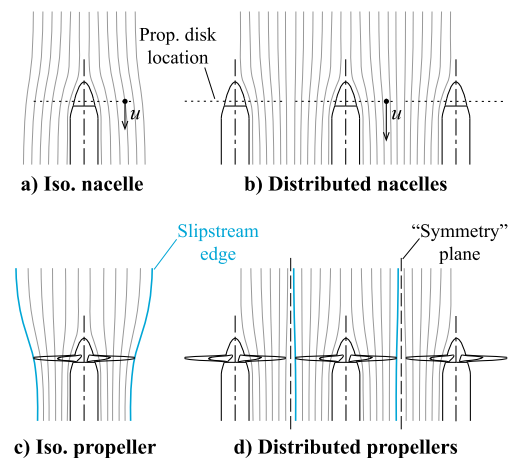


Fig. 10. Conceptual interpretation of the effect of nacelles and propellers on the streamlines in the horizontal plane ($Z = 0$).

the time-averaged loading on the propellers, but also the unsteady loading. It is also important to note that this unsteady loading exists in the blade reference frame purely as a consequence of the time-averaged influence of the adjacent slipstreams, and does not yet consider additional unsteady effects due to the perturbations produced by discrete blade passages (see Sec. 4.5).

3.2.2. Slipstream characteristics

The asymmetric inflow conditions lead to non-uniform loading on the propeller disk in the distributed configuration. This is reflected in the total-pressure distribution immediately behind the propeller disk ($X/R = 0.2$), shown in Fig. 11. These distributions do not directly represent the loading distribution on the propeller disk, due to slipstream contraction, swirl, and diffusion and dissipation in the blade wakes and tip vortices. However, they provide a qualitative description of the loading on the disk itself. The total-pressure distribution in the baseline, co-rotating configuration (Fig. 11a) shows that, overall, the propeller loading is still relatively axisymmetric. However, the interaction effects become more prominent when analyzing the changes in loading due to the presence of adjacent propellers, shown in Figs. 11b and 11c. These

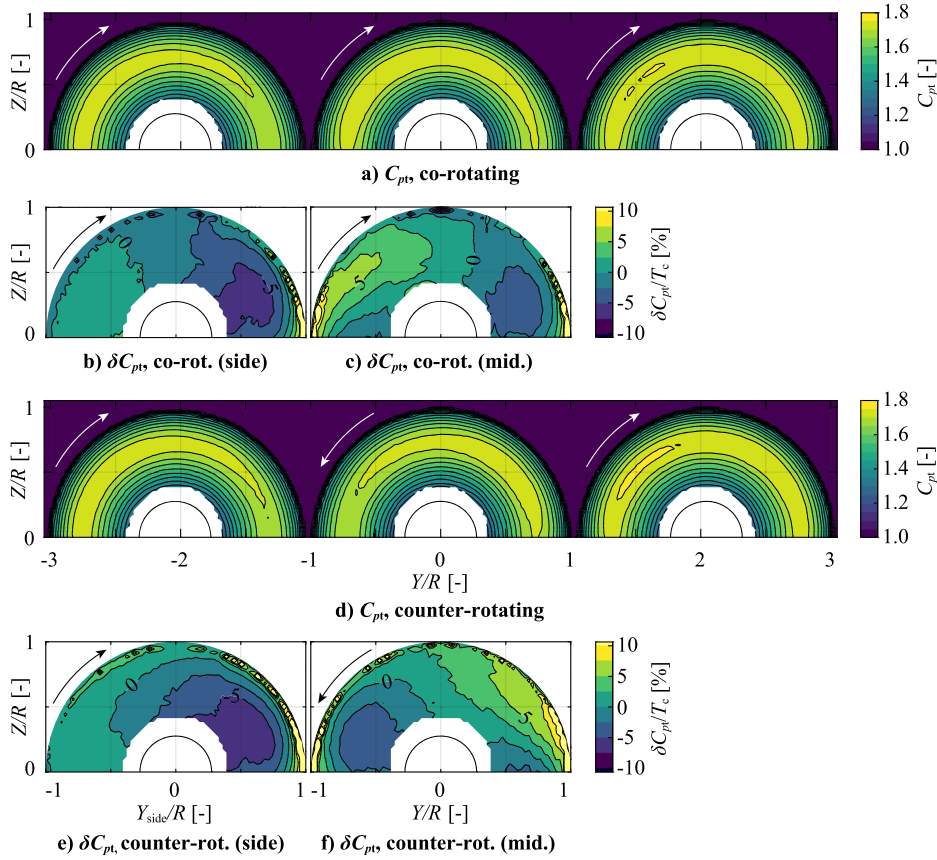


Fig. 11. Total-pressure distributions 0.2R downstream of the propellers, viewed from behind.

figures show the difference in C_{pt} between the distributed configuration and a three-nacelles, one-propeller configuration. The differences are not expressed relative to the isolated propeller, to decouple the effect of the adjacent propellers on the unsteady loading from the effect of the nacelles. Moreover, in this way, it is possible to install a single propeller on the side nacelle, and register the “deltas” on the side propeller (Fig. 11b) as well. The differences in total pressure, δC_{pt} , are normalized with the propeller thrust coefficient T_c to express the changes as a percentage of the average loading on the propeller disk.¹ Fig. 11c shows that the loading is reduced when approaching the horizontal position, especially near the radial location of highest loading ($r/R \approx 0.7$). When the blade retreats from the horizontal axis, the loading increases, especially in the outboard portion of the blade. This is consistent with the trends in blade loading observed in earlier studies [23], and is a consequence of the tangential inflow velocities seen in Fig. 8b. The magnitude of the changes in momentum is of the order of $\pm 5\%$ of the propeller thrust coefficient. On the side propeller (Fig. 11b), the same effect is observed when the blades approach the middle propeller. In this case, no significant loading changes exist in the left-hand side of the figure, since there is no adjacent propeller. In the counter-rotating case (Figs. 11d–11f), the effects on the middle propeller are mirrored, as discussed in Sec. 4.1.

It should be noted that the large changes in loading at the edges of the slipstream in Figs. 11b and 11c are not representative of local changes in blade loading. Although the loading at the blade tips might locally increase when approaching a blade or tip vortex of the adjacent propellers (see Sec. 4.5), this effect cannot be quan-

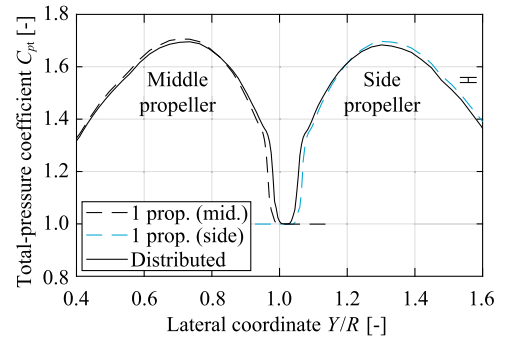


Fig. 12. Total-pressure profiles in the horizontal plane ($Z = 0$) 0.2R behind the propellers, comparing the single-propeller (with three nacelles) and distributed ($\Delta\phi = 0^\circ$) configurations.

tified with these measurements. Instead, these sharp gradients at the edge of the slipstream are mainly an artifact of the changes in slipstream contraction between the distributed-propeller and single-propeller configurations. This is shown in Fig. 12, which represents the total-pressure distribution measured in the Y -direction at $Z = 0$ with increased spatial resolution near the slipstream edge. The dashed lines show how the slipstream edge is closer to the propeller axis when a single propeller is installed on either the middle or side nacelle. However, in the distributed configuration, the quasi-symmetry condition discussed in Sec. 3.2.1 prevents slipstream contraction from occurring in the horizontal plane, and thus the edges of the slipstreams are closer to each other.

Fig. 11a shows that, at $X/R = 0.2$, the slipstreams are practically circular in cross section. Additional total-pressure distributions, not shown here, indicated that the slipstream deformation was also minor at more downstream locations. To verify the im-

¹ If the swirl component is neglected, the average total-pressure increase across the propeller is equal to its thrust coefficient: $C_{pt,mean} - C_{pt,\infty} = T_c$, where $C_{pt,\infty}$ is the freestream total-pressure coefficient ($C_{pt,\infty} = 1$).

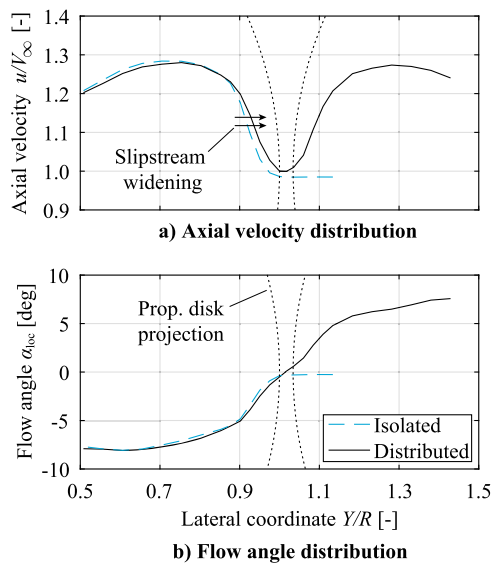


Fig. 13. Axial velocity and flow-angle profiles in the horizontal plane ($Z = 0$), $1.2R$ downstream of the propellers.

part of this minor slipstream deformation on the inflow to a downstream wing, Fig. 13 shows the axial-velocity and flow-angle distributions in the horizontal plane at $X/R = 1.2$, which can be considered a typical position of the wing leading edge. Fig. 13 shows that the maximum axial velocity in the slipstream is reduced with respect to isolated conditions. This is caused by the reduction in thrust on one hand, and the widening of the slipstream on the other. The latter is visible toward the edge of the slipstream ($Y/R \rightarrow 1$), where the velocity in the slipstream tends to freestream values faster in the isolated propeller case than in the distributed-propeller case. This distributes the momentum imparted by the propeller over a wider area. Moreover, no significant changes in inflow angle due to slipstream swirl (Fig. 13b) are observed. Therefore, the effect of propeller-propeller interaction on the integral lift of a downstream wing is expected to be minor.

4. Influence of design parameters & operating conditions on interaction effects

Now that the main interaction phenomena and their effect on the time-averaged performance of the propeller have been presented, this section describes how these phenomena are affected by different operating conditions or design choices. The influence of rotation direction, angle of attack, stagger, differential thrust, and relative phase angle is described in Secs. 4.1–4.5, respectively.

4.1. Rotation direction

To determine whether the rotation direction has a significant effect on the performance of distributed propellers, Fig. 14 presents the changes in propeller performance due to interaction for the co- and counter-rotating cases. The plots indicate the change in thrust or efficiency as a percentage of the isolated propeller's thrust or efficiency, respectively, versus the thrust setting of the isolated propeller. In all cases, there is a drop in propeller thrust and efficiency due to the interaction, which is more pronounced at lower thrust settings. This occurs because the adjacent nacelles are the main cause of the thrust reduction in the distributed configuration (see Sec. 3.2.1), and their relative contribution to the overall propeller performance is larger at lower thrust settings. The asymptotic behavior at $T_{c,iso} \rightarrow 0$ is a result of a finite change in thrust due to interaction at the advance ra-

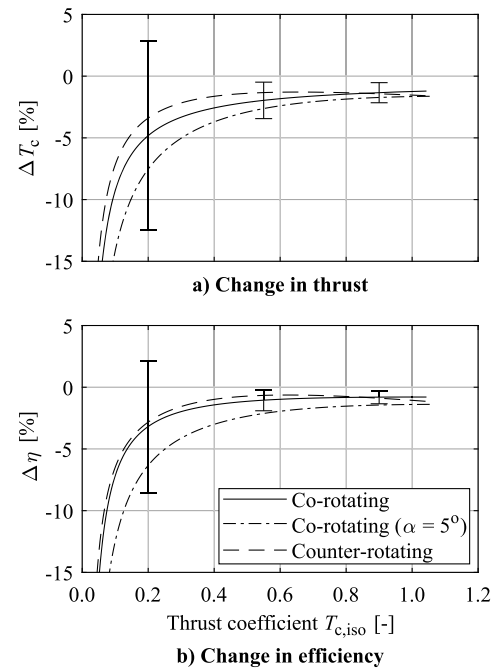


Fig. 14. Effect of rotation direction and angle of attack on the change in propeller thrust and efficiency due to interaction. Error bars are only shown for the baseline configuration, but are indicative for all cases.

tio corresponding to zero isolated-propeller thrust, as can be extrapolated from Fig. 6. For both rotation directions, the efficiency loss is approximately 1.5% at the thrust setting of maximum efficiency, $T_c = 0.38$. However, considerably lower thrust coefficients ($T_c < 0.2$) were obtained in cruise conditions in recent design activities of distributed-propeller aircraft [7,43]. Fig. 14 shows that the efficiency loss is significantly larger in those conditions, exceeding 5%. Nonetheless, as mentioned earlier, this is a result of this specific blade-pitch setting, and can be avoided in practice by selecting a blade pitch which presents the maximum efficiency at the cruise thrust setting instead.

When comparing the co- and counter-rotating cases in Fig. 14, the differences lie well within the 95% confidence interval, and are most likely related to the uncertainty of the fit and minor differences between the geometries of the two mirrored propeller models. Therefore, the effect of rotation direction on the performance penalty is negligible. This reaffirms the time-averaged interpretation of the interaction effects described in Sec. 3.2.1, according to which the rotation direction should not affect the performance of the adjacent propeller. This is further confirmed in the wake-pressure distributions, displayed in Fig. 11. When changing the rotation direction of the middle propeller, the changes in loading distribution are mirrored, and no significant change in the amplitude or extent of the peaks is observed. The loading distributions on the side propellers, meanwhile, are barely affected by the rotation direction of the middle propeller.

4.2. Angle of attack

Fig. 14 shows that the performance loss due to interaction at $\alpha = 5^\circ$ is comparable to $\alpha = 0^\circ$, though slightly more pronounced. For $\alpha = 5^\circ$, the efficiency loss at $T_c = 0.38$ is approximately 3%. A more pronounced difference can be seen in the normal-force coefficient, presented in Fig. 15. This figure shows that the normal force coefficient C_N (normalized with the rotational speed of the propeller) increases linearly with advance ratio, presenting an additional offset in the distributed configuration. This constant offset indicates that the increase in normal-force coefficient is not de-

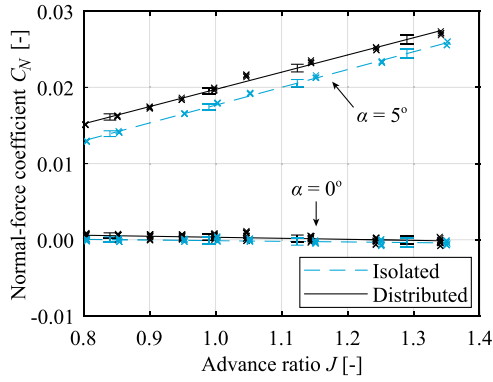


Fig. 15. Influence of interaction effects on propeller normal force. Markers indicate individual measurements.

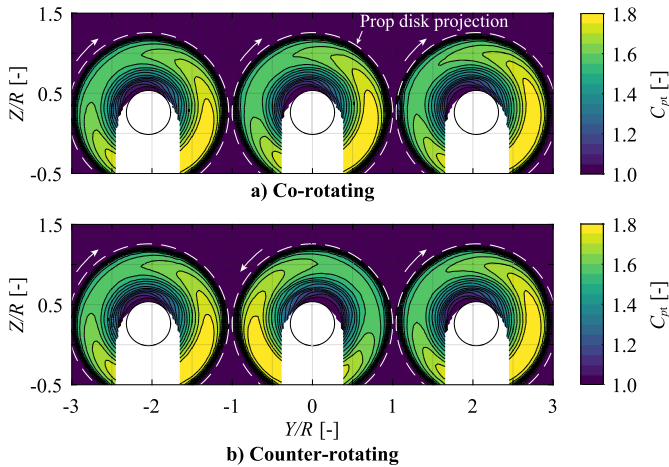


Fig. 16. Wake total-pressure distributions at $\alpha = 5^\circ$ ($X/R = 1.2$), viewed from behind. Note that the Z -coordinate is expressed relative to default reference system with propeller at $\alpha = 0^\circ$.

pendent on the slipstream contraction of the adjacent propellers. Instead, it is attributed to the presence of the adjacent nacelles, which induce an additional upwash and increase the effective angle of attack of the propeller. At the advance ratio corresponding to maximum efficiency ($J = 1.04$, $T_c \approx 0.38$), the normal force is approximately 11% higher in the distributed configuration, for an angle of attack of 5° . Therefore, the derivative $\partial C_N / \partial \alpha$ is higher in the distributed configuration, which affects aircraft stability.

The normal force is a consequence of the differences in loading between the up-going and down-going blade sides. This loading difference is reflected in the wake-pressure distributions downstream of the propeller, shown in Fig. 16. The figures show a clear non-uniform loading due to the angle of attack, where the loading is increased on the down-going blade side, and reduced on the up-going side. Given that the query plane is relatively far downstream ($X/R = 1.2$), the azimuthal regions with highest and lowest loading have been shifted in the direction of propeller rotation, due to the swirl in the slipstream on one hand, and the phase delay in unsteady blade forces on the other. Moreover, the side and middle propellers exhibit a similar loading distribution, indicating that the non-uniform loading due to the positive angle of attack is dominant over the interaction effects with neighboring propellers. Analogously to $\alpha = 0^\circ$, at $\alpha = 5^\circ$ a change in the rotation direction of the middle propeller leads to a mirrored loading distribution, and the slipstreams remain practically undeformed.

4.3. Stagger

When the propellers are placed at different axial locations, the quasi-symmetry condition described in Sec. 3.2.1 is lost. In this case, the inflow to the propeller depends, among other factors, on whether it is placed behind or ahead of adjacent propellers. This is shown in Fig. 17, which presents the velocity distributions upstream of the propellers in a forward stagger configuration, i.e. where the middle propeller is placed further forward at $X/R = -0.2$, while the side propellers remain at $X/R = 0$ (see Fig. 1e). Fig. 17a shows that the inflow to the middle is comparable to the baseline configuration without stagger (Fig. 7b). However, the contours show a slightly higher velocity magnitude, due to the axial velocity induced upstream by the adjacent propellers (see Fig. 9). Moreover, the velocity vectors near the $Y/R = 1$ plane present a weak lateral velocity component. This occurs because, for $X/R < -0.4$, the radial velocities induced by the middle propeller's vortex system dominate over the radial velocities produced by the adjacent vortex systems, since the middle propeller is placed more upstream. The downstream (side) propeller, on the other hand, experiences a significantly different inflow (Fig. 17b). Firstly, the inflow velocity magnitude is reduced. Secondly, there is a strong lateral velocity component upstream of the propeller, opposite to the usual slipstream contraction. This is visible in the horizontal plane of Fig. 17b and occurs because, upstream of the side propeller, the flowfield is dominated by the contraction of the middle (forward) propeller. This is also evident in the XZ plane, where a local region of increased velocity magnitude is visible around $X/R = -0.4$.

The resulting variations in propeller loading are illustrated by the total-pressure distributions of Figs. 18a–18f. Note that the forward propellers are installed $0.2R$ further upstream than in the baseline configuration, while the wake survey plane remains at the same location, as reflected in Fig. 1. Therefore, the measured total-pressure distribution deviates slightly more from the actual loading on the propeller disk, due to the dissipation, diffusion, and slipstream rotation that takes place between the propeller plane and the measurement plane. Again, when computing δC_{pt} , the three-nacelles, one-propeller measurement is taken as reference instead of the isolated propeller. When comparing the δC_{pt} distributions of the middle propeller in the forward (Fig. 18a, 18c) and backward (Fig. 18d, 18f) stagger configurations, it appears that on average the former presents less total-pressure rise than the latter. The opposite is observed for the side propellers. These observations reinforce the interpretation of Fig. 9, which shows that propellers positioned upstream of their neighbors perceive an increased axial inflow velocity, while the opposite occurs for propellers placed downstream of their neighbors.

However, the total-pressure distributions should be interpreted with caution, since the slipstream contraction is different between the distributed and single-propeller configurations. This is evident in Figs. 18c and 18e, which show high total-pressure values at the edge of the slipstream. These streaks appear because in the distributed case, the slipstream of the upstream propeller first contracts, and is subsequently widened due to the contraction of the adjacent propellers. Hence, the slipstream is wider than in the isolated case, and therefore the “delta” between the two appears as highly positive in the contour maps around $Y/R = \pm 1$. It is interesting to note that the opposite does not occur on the top side of the slipstream; i.e. the slipstream widens while maintaining a constant height, rather than widening while maintaining a constant cross-sectional area. Furthermore, in the backward-staggered case (Fig. 18f), the width of the slipstream is comparable to the single-propeller case, and an increase in loading of approximately 10% of the propeller thrust is observed on the left-hand side. This indicates that the unsteady loading is higher than in the case with-

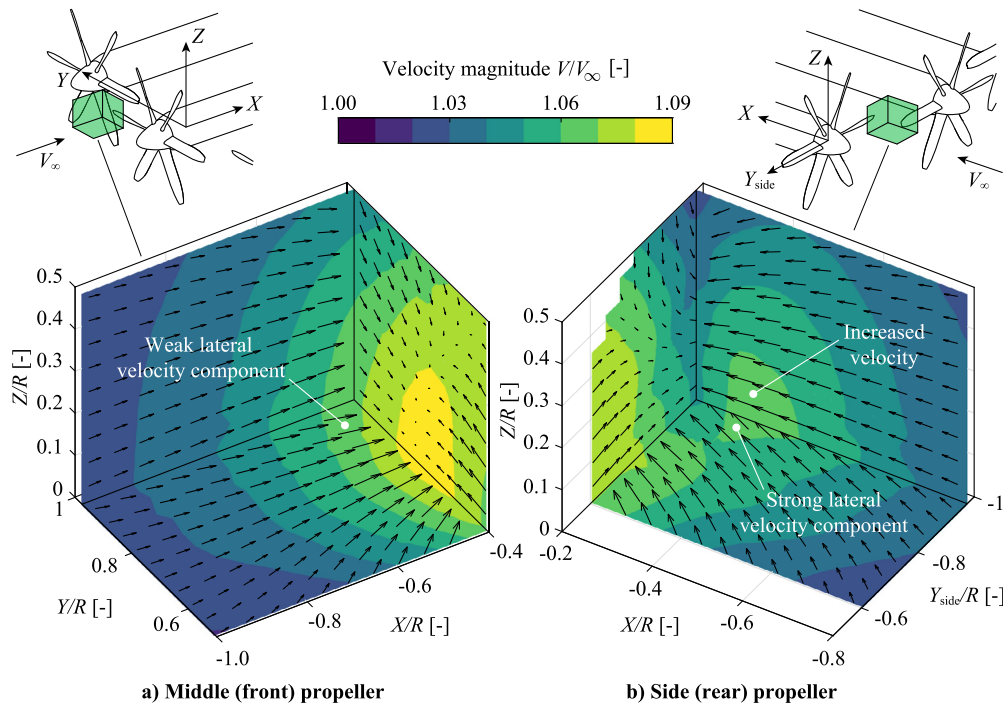


Fig. 17. Inflow velocity distributions ahead of the middle (front) propeller and side (rear) propeller in the forward-stagger configuration.

out stagger (Fig. 11c), even though the propeller blades are further away from the ones of the adjacent propellers.

The corresponding changes in propeller thrust and efficiency are shown for the different stagger configurations in Fig. 19. The differences among the various stagger configurations are comparable to the uncertainty band, and are therefore small and cannot be quantified accurately. Nonetheless, the trends are consistent with the observations made in Figs. 17 and 18. The thrust reduction of the middle propeller is largest in the forward-stagger configuration ($\Delta T_c = -4.5\%$ at $T_{c,iso} = 0.38$), due to the axial velocities induced upstream by the side propellers. The thrust and efficiency penalties of the middle propeller in the backward-staggered case are comparable to the baseline configuration, since the negative axial velocities induced by the adjacent vortex systems are partially compensated by the velocity increase due to blockage of the adjacent nacelles. Note that the effect would be opposite when staggered propellers are installed with an overlap, in which case the thrust of the downstream propeller is significantly reduced [31]. Finally, in the staired configuration, the performance loss is halfway between the forward- and backward-staggered configurations, since the effects on the two sides of the propeller compensate each other.

4.4. Differential thrust

In specific situations, the thrust setting of adjacent propellers may not be equal; for example, if a failure occurs in one of the motors, or if thrust vectoring is used to control the attitude of the aircraft. In this case, the propellers which operate at a higher thrust setting will create a slipstream which acts as a dominating boundary condition for propellers at lower thrust. This can be seen in Figs. 18g–18i, which present the total-pressure distribution in the backward-stagger configuration when the middle propeller operates at a lower thrust setting. During the wind-tunnel campaign, the impact of differential thrust was only evaluated for the backward-stagger configuration, since the interaction effects were expected to be most critical in that condition. In this case, the change in disk loading relative to the single-propeller configura-

tion is much larger than in the equal-thrust case, as shown in Fig. 18i. This leads to an increased ratio between the unsteady and steady blade loads, and occurs because the influence of the middle propeller on the flowfield is relatively weak, and thus its inflow conditions are governed by the adjacent vortex systems. For the backward-staggered configuration, this leads to deceleration of the axial inflow velocity to the middle propeller. However, the average loading on the propeller is not significantly affected, as reflected in the propeller thrust curves that are obtained when the advance ratio of the propeller is varied while maintaining the advance ratio of the side propellers constant ($J = 1.0$). This is visible in Fig. 19, which shows a small increase in thrust at low thrust settings, when compared to the backward-staggered configuration at equal thrust. At high thrust settings, the opposite occurs, since in that case the thrust of the middle propeller is higher than the thrust of the side propellers.

4.5. Relative phase angle

The relative blade phase angle between adjacent propellers, $\Delta\phi$, has an important effect on noise production, as discussed in Sec. 5. However, Fig. 20 shows that the effect on the time-averaged propeller performance is negligible. In both the co- and counter-rotating cases, the variation in propeller thrust with $\Delta\phi$ is less than 0.5% of the mean thrust. However, in the counter-rotating case, a weak sinusoidal trend can be observed. Two observations can be made in this regard. Firstly, the maximum and minimum thrust are not generated when the blades present the minimum (0°) or maximum (30°) phase difference, but at 10° and 40° . This phase delay is attributed to the evolution of the trailing vorticity that emanates from the adjacent propellers' blades, which requires some time to concentrate in the tip (and root) vortices. Secondly, the trend is only distinguishable in the counter-rotating case. This is likely due to the fact that, for this rotation direction, the blades of neighboring propellers locally move in the same direction. Thus, the velocities induced by one blade affect the blade of the neighboring propeller for a larger part of the rotation cycle.

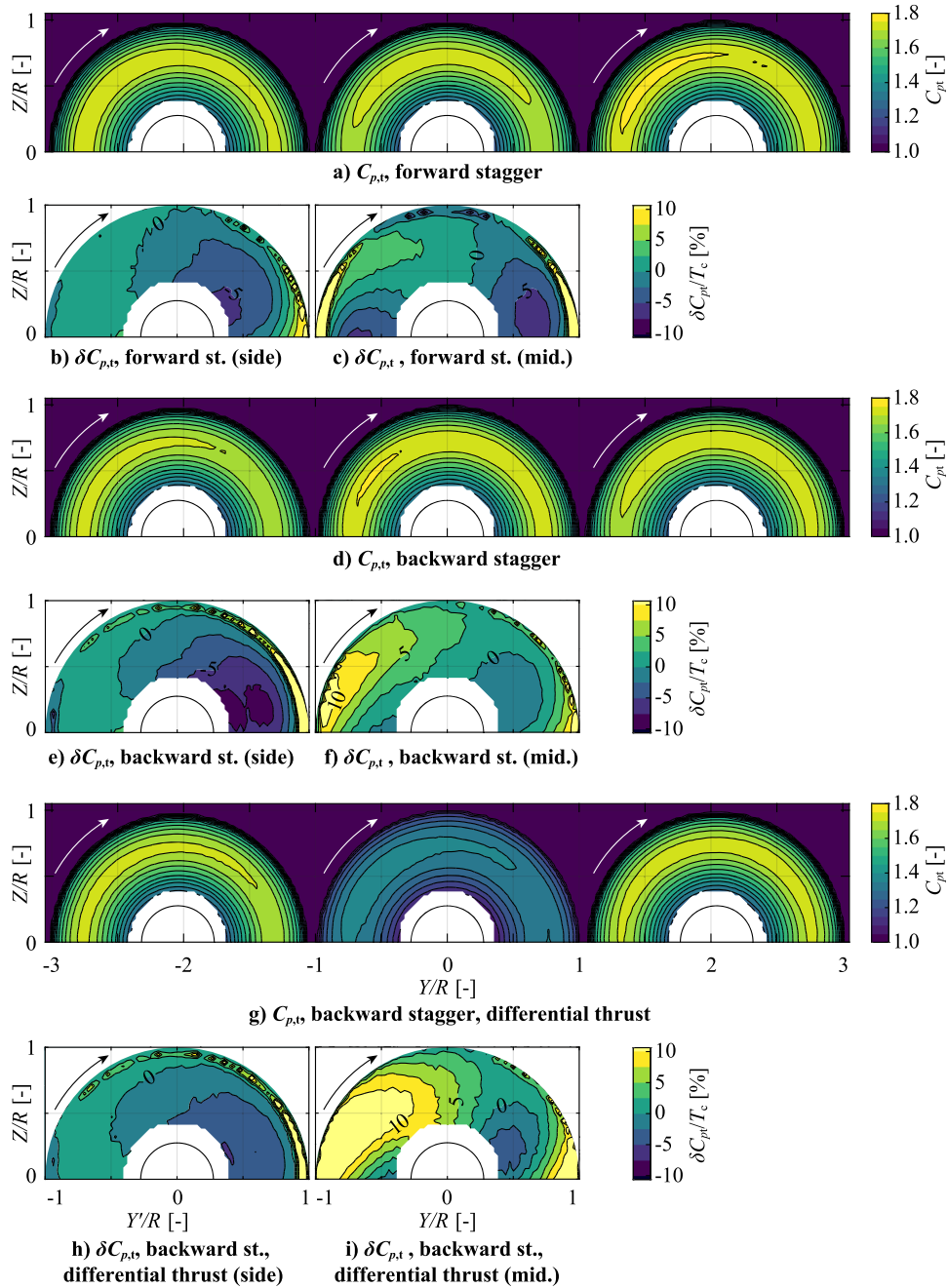


Fig. 18. Slipstream total-pressure distributions with forward and backward stagger ($X/R = 0.2$, $J = 1.00$, $J_{\text{differential thrust}} = 1.15$).

The relative phase angle also affects the slipstream evolution in the tip region between each pair of propellers, as reflected in Fig. 21. In the co-rotating case, the slipstream edges are deformed, being practically mirrored in the $\Delta\phi = 10^\circ$ and $\Delta\phi = 40^\circ$ cases. In the counter-rotating case, on the other hand, there are no noticeable local variations in the slipstream radius, although the slipstream edges are located more towards the left and right in the $\Delta\phi = 10^\circ$ and $\Delta\phi = 40^\circ$ cases, respectively. It is interesting to note that while the effect of relative phase-angle on propeller performance is more pronounced in the counter-rotating case, its effect on slipstream deformation is more pronounced in the co-rotating case. This is hypothesized to be due to the orientation of the helical tip vortices of adjacent propellers, which are locally parallel in the counter-rotating case, while being locally oblique in the co-rotating case—as shown in Fig. 22. In the counter-rotating case, the velocity induced locally by an initially undisturbed vortex Γ_1 at a

point P_2 on the adjacent vortex ($\vec{v}_{\text{ind},1\rightarrow 2}$) is perpendicular to that adjacent vortex Γ_2 . The reciprocal effect of Γ_2 on Γ_1 induces a velocity $\vec{v}_{\text{ind},2\rightarrow 1}$ of the same magnitude and direction, and therefore each tip vortex locally reduces the swirl velocity of the adjacent slipstream equally. To the contrary, in the co-rotating case, the velocities induced by each vortex on the other form an oblique angle, and are not perpendicular to the vortex filament. Compared to the isolated propeller, this changes the local direction of the flow and causes a shear in the vortex filaments which, on average, leads to the distorted slipstream edge observed in Figs. 21a and 21b. Furthermore, these induced velocities will change the loading at the blade tips throughout each blade passage. This effect is highly localized and therefore has no appreciable effect on the performance of the propeller, as evidenced in Fig. 20. However, it may lead to a noise increase due to impulsive changes in loading. This source of unsteady loading is different from the unsteady loading due to

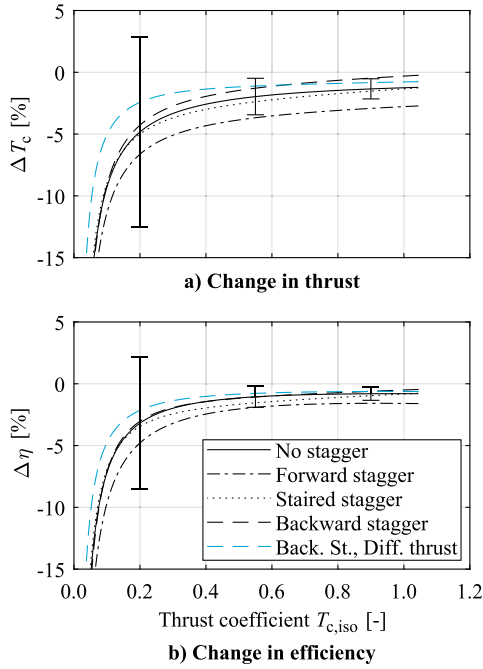


Fig. 19. Effect of stagger and differential thrust on the change in propeller thrust and efficiency due to interaction. Error bars are only shown for the baseline configuration, but are indicative for all cases.

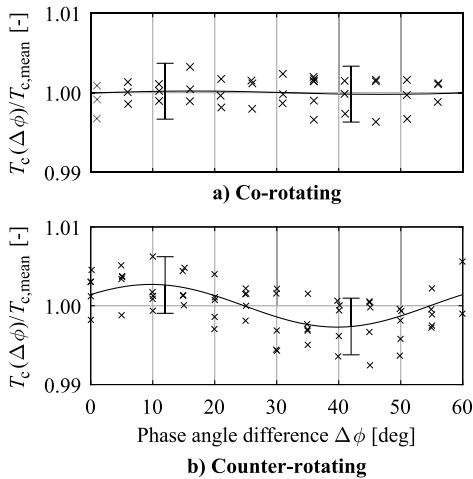


Fig. 20. Effect of relative blade-phase angle on propeller thrust. Markers indicate individual measurements.

the time-averaged tangential inflow velocities discussed in Sec. 3.2, which would also exist if the adjacent propeller were an idealized actuator disk with infinite blades. This impulsive loading on the blade tips, on the other hand, is a consequence of a repeated exposure to the same part of the unsteady flowfield induced by a finite number of blades on the adjacent propeller, rotating at a synchronized phase angle. Additional high-fidelity numerical analysis or high-resolution, unsteady measurements would be required to quantify this effect and determine how much it is affected by the relative phase angle.

5. Noise production & directivity

In order to provide a preliminary overview of the impact of the interaction effects on the noise production of the distributed-propeller system, the microphone signals were analyzed. For this, Fig. 23 compares the spectrum of a single (middle) propeller with

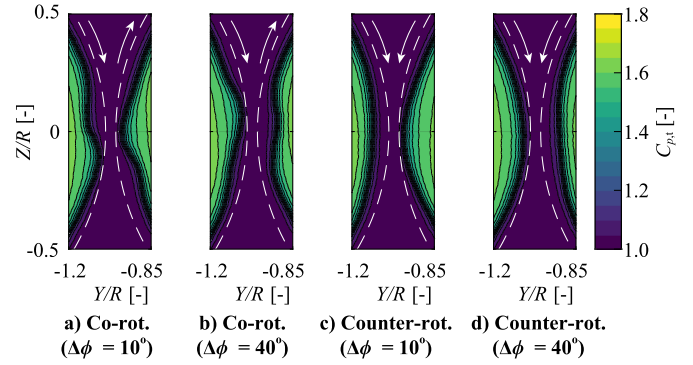


Fig. 21. Comparison of slipstream deformation for different relative phase angles ($X/R = 1.2$).

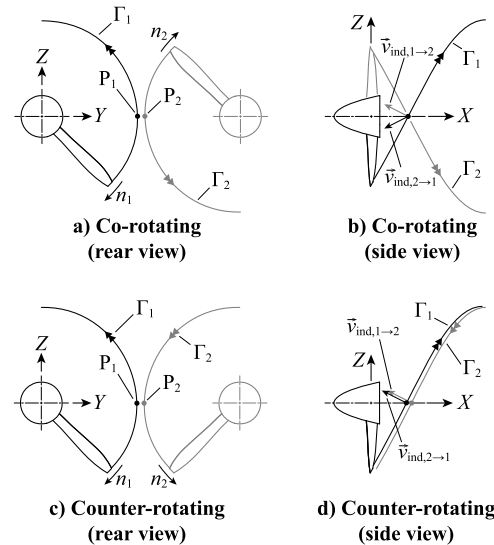


Fig. 22. Conceptual sketch of the influence of rotation direction on the velocities induced by one vortex system on the other, when the relative phase angle is kept constant ($\Delta\phi = 0^\circ$).

the spectra obtained in a distributed configuration, for two different separation distances. The data is presented at a high thrust setting ($J = 0.8$, $T_c \approx 1.04$) to improve the signal-to-noise ratio, and for a generic relative phase angle of $\Delta\phi = 0^\circ$ in the distributed configuration. In the single-propeller configuration, the nacelles of the adjacent propellers were not removed, to keep potential acoustic reflections as constant as possible in the comparison. In all cases, the tonal components at the BPF multiples are clearly visible. In the distributed-propeller configurations, not only the amplitude of the tone at the fundamental frequency is increased, but also numerous higher (sub-)harmonics appear. Moreover, when the propellers are installed in close proximity ($d/R = 0.04$), the tonal amplitude at most BPF multiples is increased. This is attributed to the increase in unsteady loading described in previous sections.

Several tonal peaks are also visible between BPF multiples in Fig. 23. These secondary peaks occur at multiples of the rotational speed ($n = \text{BPF}/6$). For single-propeller measurements, they were found to be distinguishable above the broadband levels for only some of the multiples of n , independently of which of the three propellers was being tested. For the distributed-propeller measurements, the secondary peaks were more pronounced than in the single-propeller cases, independently of the separation distance between propellers. Similar peaks at multiples of the rotational speed can be observed in previous rotor-rotor interaction studies,

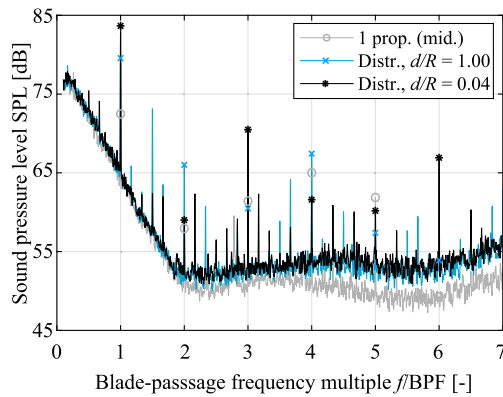


Fig. 23. Pressure spectra recorded on the wind-tunnel floor beneath the propellers ($X/R = 0$, $Y/R = 0$). Co-rotating, BPF = 1107 Hz, $J = 0.8$, $\Delta\phi = 0^\circ$.

in both anechoic [29] and non-anechoic [25] test environments. On the other hand, they were not present in recent numerical analyses [23]. Therefore, these tones may be a consequence of performing near-field noise measurements of propellers with non-uniform loading, and of a possible imbalance in the test setup, such as motor vibrations or unequal blade geometries. However, additional investigations are required to confirm the origin of these secondary peaks.

Although the trends observed in Fig. 23 were found to be representative, the amplitude of the tonal peaks is strongly dependent on the measurement location. For example, at some locations, the tone at the fundamental frequency is much lower in the distributed case, due to destructive interference between sound waves. To study this acoustic interference in more detail, Fig. 24 shows the noise pattern recorded on the wind-tunnel floor in the distributed-propeller configuration, for different relative blade-phase angles. The contours represent the change in sound pressure level based on the phase-averaged pressure waveform, p^* , rather than the raw pressure waveform. The change is expressed relative to a distribution obtained by adding up the individual SPL* contributions of the three propellers measured separately, assuming incoherent noise sources. In other words, each point presents the difference between the rms of the phase-averaged pressure waveform (p_{rms}^*) measured in the distributed-propeller configuration, and the summation of three p_{rms}^* values obtained in three separate measurements, each one with a single propeller installed on one of the three nacelles. The maps of Fig. 24 therefore represent the change in noise due to aerodynamic and acoustic interference between the propellers. These maps show that the interference leads to significant local changes in SPL*, which varies by up to ± 10 dB. These variations are larger than the differences recorded in repeated measurements (< 2.5 dB), and the trends were found to be reproducible in the experiment. Moreover, a comparison of the different relative phase angles confirms that the directivity pattern is indeed affected, as expected from earlier studies [36,37]. Due to the proximity to the noise sources and reflections on the un-treated wind-tunnel walls and propeller support elements, the patterns observed in the experiment are likely to differ significantly from the pattern that would be obtained in an actual flyover. Nevertheless, Fig. 24 confirms that phase-angle control can be used to substantially modify the radiated noise pattern.

Since the noise level is highly dependent on the sampling location, the spatial average was computed across the entire measurement area to provide an indication of the overall noise levels. Although this area is arbitrary, from Fig. 24 its size appears to be comparable to or greater than the wavelength of the noise pat-

tern.² Therefore, the size and amplitude of the lobes observed in the measurement area can be considered representative of those that would be recorded in other directions as well. Under that assumption, and considering that the measurement area captures roughly one wavelength of the pattern, the mean value in this area can be considered indicative of the overall noise level of the three-propeller system. In that case, several qualitative conclusions can be drawn by comparing the mean SPL* of different configurations. These $\text{SPL}_{\text{mean}}^*$ values are collected in Fig. 25 for the co- and counter-rotating configurations, at two separation distances. The last columns also include the summation of the three individual propellers for each case, calculated by assuming incoherent noise sources and directly adding the p_{rms}^* values recorded for each propeller separately, therefore purposefully neglecting any acoustic or aerodynamic interference. Fig. 25 shows that, in the baseline configuration (co-rotating, $d/R = 0.04$), the relative blade-phase angle changes $\text{SPL}_{\text{mean}}^*$ by ± 1.5 dB, and on average leads to an increase of approximately 1 dB relative to the three propellers separately. A similar behavior is observed for the counter-rotating case. For the case with increased separation (co-rotating, $d/R = 1.00$), only two relative phase angles were measured. The average $\text{SPL}_{\text{mean}}^*$ of the two is comparable to the summation of isolated propellers, and 1–2 dB lower than the cases with reduced separation. Furthermore, the noise patterns obtained in the case with increased separation (not shown here) indicated changes of up to ± 5 dB due to active phase control, rather than the ± 10 dB observed in Fig. 24. Several conclusions can be drawn in this regard. Firstly, the overall noise levels only increase when the propellers are placed in very close proximity, due to the aerodynamic interference—as expected from previous studies [21,23,26]. Secondly, while Fig. 24 confirms that active phase control can significantly reduce the noise at a determined location, the overall noise levels are slightly higher than three isolated propellers without interference. And thirdly, the potential benefit of phase-angle control appears to be larger for closely-placed propellers, in which case it affects not only the acoustic interference between propellers, but also the aerodynamic interference (as hypothesized in Sec. 4.5).

To distinguish between aerodynamic and acoustic interference effects, Fig. 26 presents the pressure waveforms recorded at three axial positions along the centerline of the wind tunnel. The abscissae are expressed relative to an arbitrary blade azimuth ϕ_0 , since the absolute position of the reference (middle) propeller's blades relative to the Z-axis (see Fig. 1) was unknown during these measurements. For these tonal waveforms, the phase-averaged signal was filtered to show only the contribution of the first five harmonics, since the tones of the isolated propeller practically disappear in the background noise at higher harmonics (see Fig. 23). This does not substantially affect the rms of the signal, since the first few harmonics are dominant. Two waveforms are shown in Fig. 26 for each location and configuration: the waveform recorded in the distributed configuration, and the waveform constructed artificially by adding up the waveforms of three separate measurements—each one with only one of the three propellers installed. The waveforms of the individual propellers were superimposed taking into account the phase differences between the three measurements, contrary to Fig. 24, where incoherent noise sources were assumed. The measurements with a large separation distance between the propellers (Figs. 26a, 26b) show a decent agreement between the measured waveform and the reconstructed waveform. The location and the number of peaks in the waveform are captured, although there are differences in the amplitude of the peaks. Therefore, for this configuration, the noise produced by the system can be replicated to a certain extent by simply superimposing three inde-

² Note that the dominant frequency corresponds to a wavelength of $a/\text{BPF} \approx 3R$.

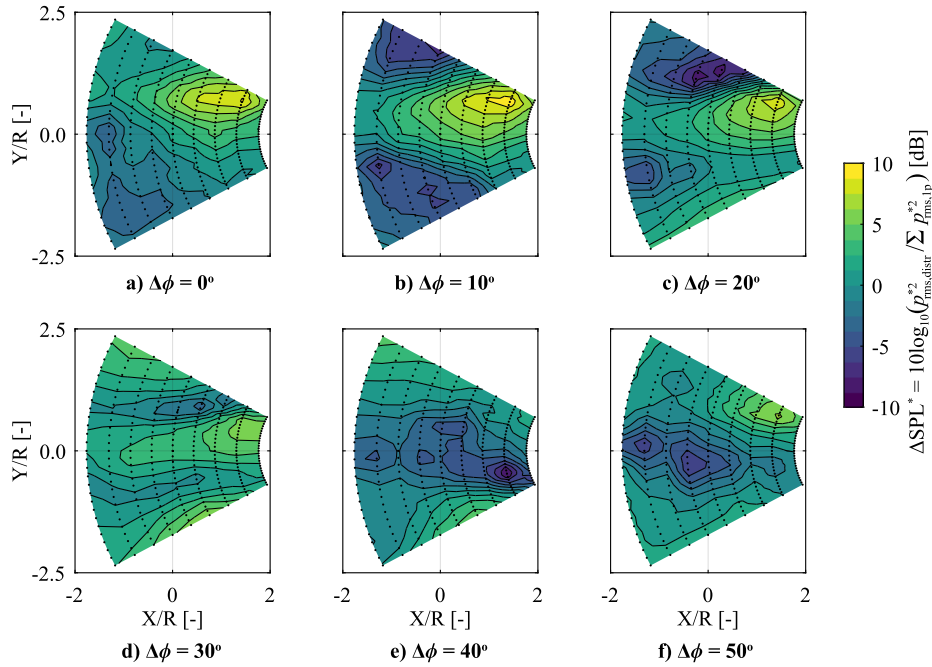


Fig. 24. Change in SPL* distribution on the wind tunnel floor ($Z/R = -6.15$) relative to the summation of three (incoherent) individual propellers. Dots indicate measurement locations. Co-rotating, $d/R = 0.04$, $J = 0.8$.

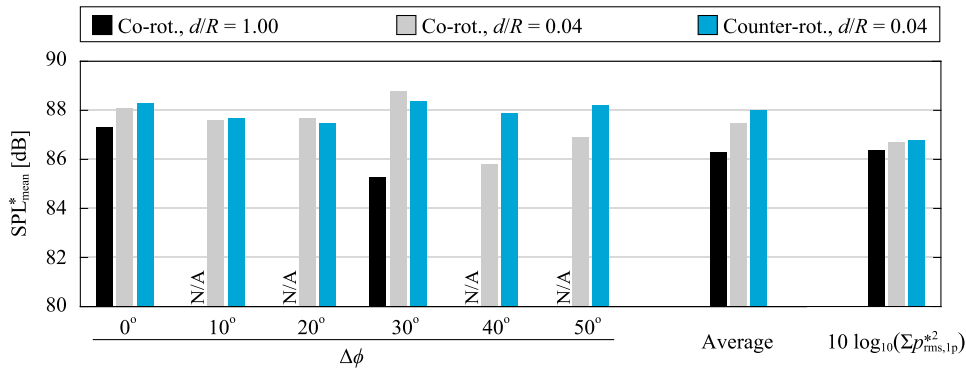


Fig. 25. Mean phase-averaged sound-pressure level, SPL_{mean}^* [dB], recorded on the area covered in Fig. 24, for different configurations and relative phase angles. "N/A" indicates the corresponding phase angle was not measured.

pendent noise sources with their corresponding phase delays. The remaining differences in the waveforms can be attributed to the uncertainty of the measurement (e.g., minor variations in atmospheric or operating conditions), a weak aerodynamic interaction between propellers, or reflections of sound waves on neighboring propellers.

When the propellers are installed in close proximity (Figs. 26c, 26d), however, the differences between the measured and reconstructed waveforms are more pronounced. This is especially visible for $\Delta\phi = 0^\circ$, where the location of the peaks has changed significantly with respect to the reconstructed waveform, and additionally sharp, high-amplitude pressure peaks are generated. These appear as higher harmonics in the pressure spectra, and show that a significant additional noise contribution is created by the unsteady aerodynamic interaction between blades of adjacent propellers. Moreover, for these measurement locations, it appears that the impulsive noise sources are present only in the $\Delta\phi = 0^\circ$ case, and not in the $\Delta\phi = 30^\circ$ case. Although this is partially a coincidence due to the selected sampling location, in general, a comparison of other measurement locations showed that the sharp peaks were more pronounced in the $\Delta\phi = 0^\circ$ case. This suggests that the unsteady loading due to the interaction effects described in

Sec. 4.5 is higher for $\Delta\phi = 0^\circ$ than for $\Delta\phi = 30^\circ$. Nonetheless, the overall noise levels of the two phase angles are comparable, as reflected in Fig. 25.

6. Conclusions & recommendations

An experimental investigation has been performed to study the interaction effects that arise when multiple propellers operate in close proximity in a distributed-propulsion configuration. To this end, the propeller performance and flow field around a propeller surrounded by two adjacent ones were measured, as well as the noise produced by the system. The results show that, for a given rotational speed, the propeller thrust and efficiency are slightly reduced in the distributed-propeller configuration, when compared to an isolated propeller. In this study, the propulsive efficiency loss due to the interaction was 1.5% at the thrust setting corresponding to maximum efficiency, for a tip-clearance equal to 4% of the propeller radius. For a given blade-pitch angle, this performance penalty is larger at lower thrust settings and is independent of the rotation direction of the propellers. It is also more pronounced at non-zero angle of attack, in which case the interaction additionally leads to an increased propeller normal force. In the present study,

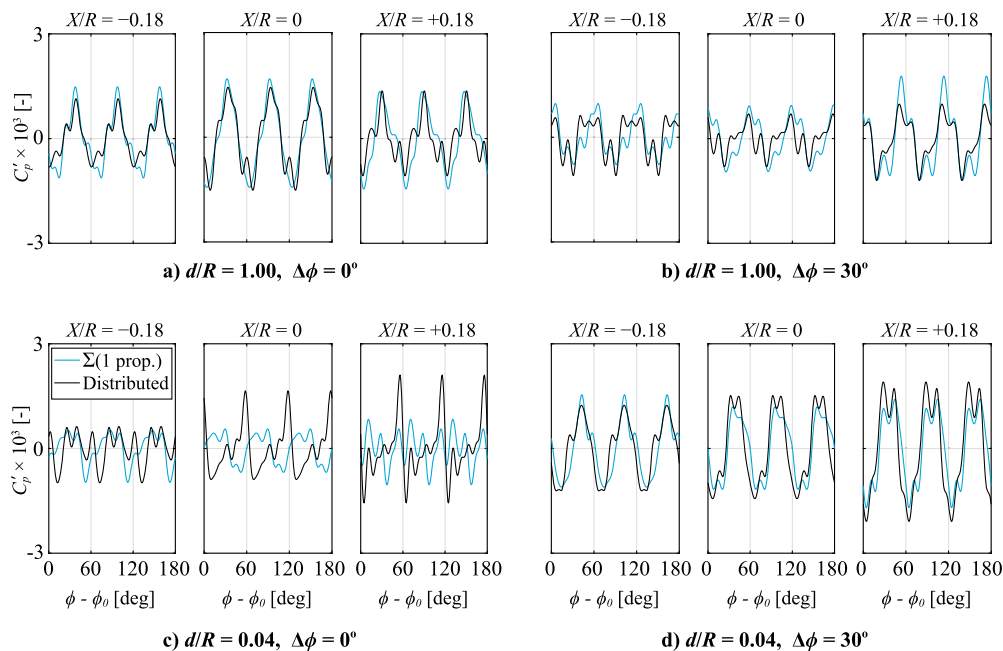


Fig. 26. Tonal waveforms recorded on the wind-tunnel floor ($Y/R = 0$, $Z/R = -6.15$), reconstructed from the first five harmonics. Co-rotating configuration.

at $\alpha = 5^\circ$, the aerodynamic interaction was found to decrease the propulsive efficiency by 3% and increase the propeller normal force by 11% at the thrust setting corresponding to maximum efficiency. The performance reduction is predominantly caused by the blockage effect of the adjacent nacelles, and is more pronounced for a propeller positioned slightly upstream of the neighboring propellers (forward stagger), while being smaller when the propeller is positioned further downstream (backward stagger).

In the no-stagger configuration, the velocities induced by the propeller blades and slipstream do not significantly affect the time-averaged performance of the adjacent propellers. However, they induce an in-plane velocity component which creates a quasi-symmetry condition halfway between each pair of propellers, and leads to loading variations across the propeller disk of 5%–10% of the average pressure jump. Therefore, the unsteady blade loading observed in earlier propeller-propeller interaction studies exists not only due to the unsteady interaction between discrete blade tips and tip vortices, but also due to the time-averaged velocities induced by the adjacent propellers' vortex system. The effect of unsteady blade-blade interaction between adjacent propellers on the time-averaged propeller forces appears to be minor, since the relative phase angle between the propellers has a negligible effect on propeller performance.

Regarding the time-averaged evolution of the slipstreams, in general, the velocity distribution in the downstream slipstream is not significantly altered by the adjacent ones. At a typical wing leading-edge location ($X/R = 1.2$), the slipstreams remain as three independent streamtubes, rather than merging to form a continuous high-momentum region, as is often assumed in literature. However, the slipstreams are slightly wider in the distributed case, and contain a non-uniform total-pressure distribution. The exact shape of the slipstream edge is dependent on the relative phase angle of the propellers.

Preliminary noise measurements confirm that, if the propellers are placed in close proximity, the overall noise levels recorded on the wind-tunnel floor in the distributed-propeller configuration are higher than three times the isolated-propeller noise levels. When the propellers are placed far from each other ($d/R = 1.00$), the tonal noise signal recorded at a given location is comparable to the

superposition of three individual propellers, corrected for the relative phase delay. When the propellers are installed in close proximity ($d/R = 0.04$), the tonal noise signal contains sharp peaks that are not captured by superimposing the three individual-propeller signals. In that case, both the acoustic interaction and the aerodynamic interaction affect the directivity pattern of the system, and the spectrum includes numerous higher harmonics. In these experiments, the interaction led to sound-pressure-level changes up to ± 10 dB at a given location. Moreover, the relative phase angle between adjacent propellers is confirmed to have a substantial effect on the directivity of the noise emissions, although the overall noise levels do not appear to be significantly affected.

Although the findings of this study provide insight into several interaction mechanisms, other aspects remain unanswered. Most importantly, the unsteady aerodynamic interaction between adjacent propeller blade tips and tip vortices should be investigated, to determine how this affects the local unsteady loading on the blades. Even though the results of this study suggest that the impact of such interaction on integral propeller performance is negligible, it is most likely relevant for the noise production of novel aircraft configurations with distributed propellers. In this sense, high-fidelity aeroacoustic analyses could provide additional insight into the noise-generation mechanism, and allow more sound conclusions regarding the far-field noise pattern. Regarding the performance of the system, these findings can be combined with propeller-wing interaction studies to determine the overall effect of distributed-propeller systems. For such studies, special attention should be paid to the effect of the nacelles. From a design perspective, a trade-off should be performed to determine whether the clearance between propellers should be increased to minimize the noise and performance penalty. In that case, the lift-enhancement capabilities on the wing and geometrical constraints may be adversely affected, so it would be important to explore the design space and determine the optimum location of the propellers along the wing. A more detailed investigation of such effects would enable more efficiently-integrated propulsion systems and, ultimately, more sustainable aircraft.

Declaration of competing interest

The authors declare that they have no known competing financial interests or personal relationships that could have appeared to influence the work reported in this paper.

Funding

This research is funded by the European Union's Horizon 2020 Clean Sky 2 Large Passenger Aircraft program (CS2-LPA-GAM-2020/2021-01).

Acknowledgements

The authors would like to thank Peter den Dulk and Ed Roessen for the manufacturing of the wind-tunnel model, and the members of the FPP Propulsion Research Group for fruitful discussions and feedback on the presented results. The authors would also like to thank Daniele Ragni for his assistance with the PIV measurements and Francesco Avallone for insightful discussions regarding the microphone data.

References

- [1] National Academies of Sciences, Engineering, and Medicine, in: *Commercial Aircraft Propulsion and Energy Systems Research: Reducing Global Carbon Emissions*, National Academies Press, 2016.
- [2] Advisory Council for Aviation Research and Innovation in Europe (ACARE), Realising Europe's vision for aviation, in: *Strategic research & innovation agenda*, Vol. 1, Advisory Council for Aviation Research and Innovation in Europe, 2012.
- [3] Strategic research and innovation agenda: the proposed European partnership for clean aviation, available online <http://www.clean-aviation.eu/>, July 2020.
- [4] B.J. Brelje, J.R.R.A. Martins, Electric, hybrid, and turboelectric fixed-wing aircraft: a review of concepts, models, and design approaches, *Prog. Aerosp. Sci.* 104 (2019) 1–19, <https://doi.org/10.1016/j.paerosci.2018.06.004>.
- [5] S. Sahoo, X. Zhao, K. Kyprianidis, A review of concepts, benefits, and challenges for future electrical propulsion-based aircraft, *Aerospace* 7 (2020) 44, <https://doi.org/10.3390/aerospace7040044>.
- [6] H.D. Kim, Distributed propulsion vehicles, in: *27th Congress of the International Council of the Aeronautical Sciences*, Nice, France, September 19–24 2010, 2010.
- [7] R. de Vries, M.F.M. Hoogref, R. Vos, Preliminary sizing of a hybrid-electric passenger aircraft featuring over-the-wing distributed-propulsion, in: *AIAA Scitech 2019 Forum*, San Diego, CA, USA, January 7–11 2019, 2019.
- [8] N.K. Borer, M.D. Patterson, J.K. Viken, M.D. Moore, S. Clarke, M.E. Redifer, R.J. Christie, A.M. Stoll, A. Dubois, J.B. Bevirt, A.R. Gibson, T.J. Foster, P.G. Osterkamp, Design and performance of the NASA SCEPTOR distributed electric propulsion flight demonstrator, in: *16th AIAA Aviation Technology, Integration, and Operations Conference*, Washington, DC, USA, June 13–17 2016, 2016.
- [9] S. Biser, M. Filipenko, M. Boll, N. Kastner, G. Atanasov, M. Hepperle, D. Keller, D. Vechtel, M. Noe, Design space exploration study and optimization of a distributed turbo-electric propulsion system for a regional passenger aircraft, in: *AIAA Propulsion and Energy, Forum (Virtual Event)*, August 24–28 2020, 2020.
- [10] A.M. Stoll, G.V. Mikić, Design studies of thin-haul commuter aircraft with distributed electric propulsion, in: *16th AIAA Aviation Technology, Integration, and Operations Conference*, Washington, DC, USA, June 13–17 2016, 2016.
- [11] E.A.P. Marcus, R. de Vries, A. Raju Kulkarni, L.L.M. Veldhuis, Aerodynamic investigation of an over-the-wing propeller for distributed propulsion, in: *2018 AIAA Aerospace Sciences Meeting*, Kissimmee, FL, USA, January 8–12 2018, 2018.
- [12] M.D. Patterson, Conceptual Design of High-Lift Propeller Systems for Small Electric Aircraft, PhD Dissertation, Georgia Institute of Technology, 2016.
- [13] C. Dornier, The Dornier Do.X Seaplane: full technical details of the design and construction of the largest flying boat yet built, *Aircr. Eng. Aerosp. Technol.* 1 (10) (1929) 339–341, <https://doi.org/10.1108/eb029211>.
- [14] R. de Vries, M.F.M. Hoogref, R. Vos, Aeropropulsive efficiency requirements for turboelectric transport aircraft, in: *AIAA Scitech 2020 Forum*, Orlando, FL, USA, January 6–10 2020, 2020.
- [15] R.C. Dingeldein, Wind-tunnel studies of the performance of multirotor configurations, *NACA Technical Note* 3236, 1954.
- [16] G.E. Sweet, Hovering measurements for twin-rotor configurations with and without overlap, *NASA Technical Note* D-534, 1960.
- [17] M. Ramasamy, Hover performance measurements toward understanding aerodynamic interference in coaxial, tandem, and tilt rotors, *J. Am. Helicopter Soc.* 60 (3) (2015), <https://doi.org/10.4050/JAHS.60.032005>.
- [18] A. Bagai, J.G. Leishman, Free-wake analysis of tandem, tilt-rotor and coaxial rotor configurations, *J. Am. Helicopter Soc.* 41 (3) (1996) 196–207, <https://doi.org/10.4050/JAHS.41.196>.
- [19] C. Sheng, J.C. Narramore, Computational simulation and analysis of bell boeing quad tiltrotor aero interaction, *J. Am. Helicopter Soc.* 54 (4) (2009), <https://doi.org/10.4050/JAHS.54.042002>.
- [20] D. Barcelos, A. Kolaei, G. Bramesfeld, Aerodynamic interactions of quadrotor configurations, *J. Aircr.* 57 (6) (2020), <https://doi.org/10.2514/1.C035614>.
- [21] H. Lee, D.-J. Lee, Rotor interactional effects on aerodynamic and noise characteristics of a small multirotor unmanned aerial vehicle, *Phys. Fluids* 32 (2020), <https://doi.org/10.1063/5.0003992>.
- [22] E.J. Alvarez, A. Ning, High-fidelity modeling of multirotor aerodynamic interactions for aircraft design, *AIAA J.* 58 (10) (2020), <https://doi.org/10.2514/1.J059178>.
- [23] E.J. Alvarez, A. Schenk, T. Critchfield, A. Ning, *Rotor-on-Rotor Aeroacoustic Interactions of Multirotor in Hover*, Vol. 4053, Brigham Young University Faculty Publications, 2020.
- [24] S. Yoon, H.C. Lee, T.H. Pulliam, Computational analysis of multi-rotor flows, in: *54th AIAA Aerospace Sciences Meeting*, San Diego, CA, USA, January 4–8 2016, 2016.
- [25] W. Zhou, Z. Ning, H. Li, H. Hu, An experimental investigation on rotor-to-rotor interactions of small UAV, in: *35th AIAA Applied Aerodynamics Conference*, Denver, CO, USA, June 5–9 2017, 2017.
- [26] Z. Ning, Experimental investigations on the aerodynamic and aeroacoustic characteristics of small UAS propellers, PhD Dissertation, Iowa State University, 2018.
- [27] D. Shukla, N. Komerath, Multirotor drone aerodynamic interaction investigations, *Drones* 4 (2) (2018) 43, <https://doi.org/10.3390/drones2040043>.
- [28] D. Shukla, N. Komerath, Low Reynolds number multirotor aerodynamic wake interactions, *Exp. Fluids* 60 (77) (2019), <https://doi.org/10.1007/s00348-019-2724-3>.
- [29] C.E. Tinney, J. Sirohi, Multirotor drone noise at static thrust, *AIAA J.* 56 (7) (2018), <https://doi.org/10.2514/1.J056827>.
- [30] M. Veismann, M. Gharib, High fidelity aerodynamic force estimation for multirotor crafts in free flight, in: *AIAA Scitech 2020 Forum*, Orlando, FL, USA, January 6–10 2020, 2020.
- [31] T.C.A. Stokkermans, D. Usai, T. Sinnige, L.L.M. Veldhuis, Aerodynamic interaction effects between propellers in typical eVTOL vehicle configurations, *J. Aircr.* (2021), <https://doi.org/10.2514/1.C035814>.
- [32] W. Johnson, C. Silva, E. Solis, Concept vehicles for VTOL air taxi operations, in: *AHS Technical Conference on Aeromechanics Design for Transformative Vertical Flight*, San Francisco, CA, USA, January 16–19 2018, 2018.
- [33] G. Bernardini, F. Centracchio, M. Gennaretti, U. Iemma, C. Pasquali, C. Poggi, M. Rossetti, J. Serafini, Numerical characterisation of the aeroacoustic signature of propeller arrays for distributed electric propulsion, *Appl. Sci.* 10 (2020), <https://doi.org/10.3390/app10082643>.
- [34] M. Roger, S. Moreau, Tonal-noise assessment of quadrotor-type UAV using source-mode expansions, *Acoustics* 2 (2020), <https://doi.org/10.3390/acoustics2030036>.
- [35] K.A. Pascioni, S.A. Rizzi, Tonal noise prediction of a distributed propulsion unmanned aerial vehicle, in: *2018 AIAA/CEAS Aeroacoustics Conference*, Atlanta, GA, USA, June 25–29 2018, 2018.
- [36] K.A. Pascioni, S.A. Rizzi, A.R. Aumann, Auralization of an unmanned aerial vehicle under propeller phase control, in: *INTER-NOISE and NOISE-CON Congress and Conference Proceedings*, Vol. 258(7), 2018, pp. 421–431.
- [37] K.A. Pascioni, S.A. Rizzi, N.H. Schiller, Noise reduction potential of phase control for distributed propulsion vehicles, in: *AIAA Scitech 2019 Forum*, San Diego, CA, USA, January 7–11 2019, 2019.
- [38] B. Magliozzi, Synchrophasing for cabin noise reduction of propeller-driven airplanes, in: *8th Aeroacoustics Conference*, Atlanta, GA, USA, April 11–13 1983, 1983.
- [39] J.F. Johnston, R.E. Donham, W.A. Guinn, Propeller signatures and their use, *J. Aircr.* 18 (11) (1981) 934–942, <https://doi.org/10.2514/3.57583>.
- [40] S.A. Rizzi, D.L. Palumbo, J. Rathsam, A. Christian, M. Rafaelof, Annoyance to noise produced by a distributed electric propulsion high-lift system, in: *23rd AIAA/CEAS Aeroacoustics Conference*, Denver, CO, USA, June 5–9 2017, 2017.
- [41] A. Patterson, A. Gahlawat, N. Hovakimyan, Propeller phase synchronization for small distributed electric vehicles, in: *AIAA Scitech 2019 Forum*, San Diego, CA, USA, January 7–11 2019, 2019.
- [42] A. Patterson, K. Ackerman, A. Gahlawat, N. Hovakimyan, N.H. Schiller, I. Gregory, Controller design for propeller phase synchronization with aeroacoustic performance metrics, in: *AIAA Scitech 2020 Forum*, Orlando, FL, USA, January 6–10 2020, 2020.
- [43] R. de Vries, M. Brown, R. Vos, Preliminary sizing method for hybrid-electric distributed-propulsion aircraft, *J. Aircr.* 56 (6) (2019) 2172–2188, <https://doi.org/10.2514/1.C035388>.
- [44] L. Ting, C.H. Liu, G. Kleinstein, Interference of wing and multipropellers, *AIAA J.* 10 (7) (1972) 906–914, <https://doi.org/10.2514/3.50244>.
- [45] J. Serpieri, Cross-Flow Instability: Flow diagnostics and control of swept wing boundary layers, PhD Dissertation, Delft University of Technology, 2018.

- [46] N. van Arnhem, R. de Vries, T. Sinnige, R. Vos, G. Eitelberg, L.L.M. Veldhuis, Engineering method to estimate the blade loading of propellers in nonuniform flow, *AIAA J.* 58 (12) (2020) 5332–5346, <https://doi.org/10.2514/1.J059485>.
- [47] N. van Arnhem, R. de Vries, T. Sinnige, R. Vos, L.L.M. Veldhuis, Aerodynamic performance and static stability characteristics of tail-mounted propeller aircraft, *J. Aircr.* (2021), manuscript under review.
- [48] R. de Vries, N. van Arnhem, F. Avallone, D. Ragni, R. Vos, G. Eitelberg, L.L.M. Veldhuis, Experimental investigation of over-the-wing propeller–boundary-layer interaction, *AIAA J.* 59 (6) (2021) 2169–2182, <https://doi.org/10.2514/1.J059770>.
- [49] B.F.R. Ewald (Ed.), *Wind Tunnel Wall Corrections (la Correction des effets de paroi en soufflerie)*, Advisory Group for Aerospace Research and Development AGARD-AG-336, 1998.
- [50] B. Wieneke, PIV uncertainty quantification from correlation statistics, *Meas. Sci. Technol.* 26 (2015) 074002, <https://doi.org/10.1088/0957-0233/26/7/074002>.
- [51] T. Sinnige, B. Della Corte, R. de Vries, F. Avallone, R. Merino Martinez, D. Ragni, G. Eitelberg, L.L.M. Veldhuis, Alleviation of propeller-slipstream-induced unsteady pylon loading by a flow-permeable leading edge, *J. Aircr.* 56 (3) (2019) 1214–1230, <https://doi.org/10.2514/1.C035250>.
- [52] L.R. Miranda, J.E. Brennan, Aerodynamic effects of wingtip-mounted propellers and turbines, in: 4th Applied Aerodynamics Conference, San Diego, CA, USA, June 9-11 1986, 1986.
- [53] M.P. Metcalfe, On the modelling of a fully-relaxed propeller slipstream, in: *AIAA/SAE/ASME/ASEE 21th Joint Propulsion Conference*, Monterey, CA, USA, July 8-10 1985, 1985.
- [54] L.L.M. Veldhuis, *Propeller Wing Aerodynamic Interference*, PhD Dissertation, Delft University of Technology, 2005.